

Vertical autofocus for the phase screen in a turbulent ionosphere

Mikhail Gilman*  and Semyon Tsynkov 

Department of Mathematics, North Carolina State University, Raleigh, NC 27695,
United States of America

E-mail: mgilman@ncsu.edu

Received 10 February 2022; revised 28 October 2022

Accepted for publication 3 February 2023

Published 2 March 2023



CrossMark

Abstract

The performance of spaceborne synthetic aperture radars (SARs) is affected by the Earth's ionosphere. In particular, the ionospheric turbulence causes phase perturbations of the SAR signals, which may lead to image distortions. A convenient way to model those phase perturbations is by means of a phase screen. The latter is an infinitesimally thin layer positioned at a certain elevation above the Earth's surface. The radar signal acquires an instant perturbation once its trajectory intersects the screen. The trajectory is a ray between the antenna and the target, and the magnitude of the perturbation is equal to the screen density at the intersection point. The density is a bivariate function of the coordinates along the screen. The coordinates of a specific intersection point are determined by the ray itself, as well as the screen elevation. Thus, the magnitude of the phase perturbation explicitly depends on the screen elevation. Accordingly, to compensate for the resulting image distortions one should be able to determine the elevation of the screen. In the paper, we develop an algorithm of vertical autofocus that derives this elevation from the received SAR data, given a pair of point scatterers in the target area. The proposed algorithm exploits a modification of the coherent interferometric imaging that was previously employed to reduce the effect of phase errors due to the trajectory uncertainty. In our analysis, we highlight the differences between this case and transionospheric propagation.

* Author to whom any correspondence should be addressed.



Original Content from this work may be used under the terms of the [Creative Commons Attribution 4.0 licence](https://creativecommons.org/licenses/by/4.0/). Any further distribution of this work must maintain attribution to the author(s) and the title of the work, journal citation and DOI.

Keywords: spaceborne synthetic aperture radar,
coherent interferometric (CINT) imaging, phase screen elevation

(Some figures may appear in colour only in the online journal)

1. Introduction

Synthetic aperture radar (SAR) images are maps of backscattering reflectivity of the targets. These images are obtained by recording and (digitally) processing the radar pulses reflected off the target. Processing of the SAR signals requires a great degree of consistency in the measurements of certain distance and time parameters. Significant distortions of SAR images can be observed if this consistency is not maintained.

For example, whereas for a spaceborne radar, the length of a synthetic aperture is many kilometers and the distance between the antenna and the target is many hundreds of kilometers [1], the uncertainty in the variation of the signal travel distance over the aperture should be small compared to the radar wavelength, which is in the range from several centimeters to one meter. At the same time, the propagation of radar signals in the ionosphere is dispersive. Dispersion causes the deviation of both the phase and group velocity from the speed of light. The deviation is proportional to the electron number density [2–4], which exhibits spatial variations, largely due to the ionospheric turbulence. Thus, turbulent fluctuations of the electron density translate into the phase perturbations of radar signals traveling through the ionosphere. The latter need to be carefully taken into account for SAR signal processing.

In general, the effect of the ionosphere on spaceborne SAR imaging becomes stronger as the carrier frequency of the SAR sensor decreases [4–7]. At the same time, it is the lower frequencies, e.g. P-band, that offer a better foliage and ground penetrating capability [1, 8]. Therefore, the SAR missions that may require this capability are also those most susceptible to ionospheric distortions. This applies, in particular, to the BIOMASS satellite (to be launched in the near future) that carries a low-frequency radar instrument [2, 4, 8, 9].

The actual Earth's ionosphere is a layer of plasma several hundreds of kilometers thick. Yet for the purpose of modeling the transionospheric SAR, one can conveniently represent it using a phase screen¹. Mathematically, the phase screen is an infinitely thin layer positioned at a certain elevation above the Earth's surface. The screen is characterized by its density, a bivariate function. The phase perturbation for each signal is the value of the density at the intersection of the signal trajectory with the screen.

Consider a simplified geometry of transionospheric imaging where the imaged scene consists of a single isolated point scatterer and the trajectory of the radar platform (satellite orbit) is an interval of a straight line, see figure 1 and [4, section 3.3]. With no ionosphere, a SAR signal processing algorithm², known as the matched filter [10, 11], builds images of the target by compensating the signal travel phase. The travel phase is proportional to the distance R_z between the antenna and the scatterer. If x and z are the respective horizontal coordinates of the former and the latter, then

$$\text{travel phase} = \frac{2\pi}{\lambda} \cdot 2R_z, \quad \text{where} \quad R_z \approx R + \frac{(x-z)^2}{2R}. \quad (1)$$

¹ A quantitative justification for the use of this representation will be provided in a future work.

² The application of SAR signal processing is also referred to as focusing.

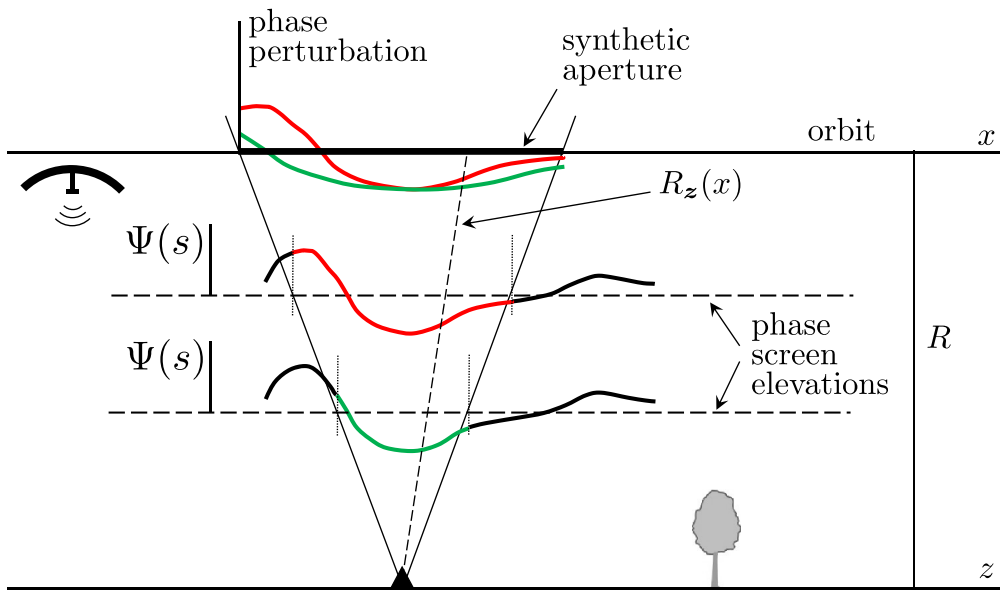


Figure 1. Uncertainty of the phase screen elevation leads to the ambiguity of the phase perturbation term. For one and the same screen density $\Psi(s)$ (black curves with red and green inserts), two possible screen elevations shown by the horizontal dashed lines yield two different realizations of the perturbation to be corrected (red and green curves on the top).

In (1), λ is the radar wavelength and R is the distance between the scatterer and the orbit. Besides, it is assumed that the length of the synthetic aperture is much shorter than R so that the leading order of the Taylor approximation for R_z would suffice.

Denote by ξ the screen elevation relative to the orbit elevation, $0 < \xi \leq 1$. The intersection of the phase screen with the plane containing the orbit and the scatterer is a horizontal line, see figure 1. Let $\Psi = \Psi(s)$ be the screen density along this line. Then, the overall phase to be compensated by matched filtering becomes

$$\begin{aligned} \text{total phase} &= \text{travel phase} + \text{perturbation} \\ &= \frac{2\pi}{\lambda} \cdot 2R_z - \psi(x, z), \end{aligned} \tag{2}$$

where

$$\psi(x, z) = \Psi(\xi x + (1 - \xi)z) \tag{3}$$

and for convenience, Ψ denotes the phase perturbation due to two crossings of the screen³.

Formula (3) indicates that the phase perturbation at every x depends on the elevation of the phase screen ξ . In addition, figure 1 illustrates how the uncertainty in the value of ξ translates into the uncertainty in the phase correction term. We can therefore conclude that knowing ξ is important for compensating the turbulent phase perturbations. In the literature, the elevation

³ For the choice of sign at ψ in (2), see the footnote on page 5.

of the phase screen ξ is sometimes attributed to the altitude where the maximum mean (i.e. non-turbulent) electron number density is achieved, about 350 km above the Earth's surface [3, 12, 13]. In reality though, the turbulent phenomena that define the phase screen may take place at a different altitude [3, 14]. Hence, to mitigate the ionospheric distortions, one needs to be able to determine the screen elevation ξ that corresponds to the state of the ionosphere at a time of image acquisition.

In this work, we present a methodology for retrieving the value of ξ using a modification of coherent interferometric (CINT) imaging [15–18]. In the context of phase perturbations, CINT is different from SAR in that it requires neither a reconstruction nor correction of those. Instead, it is assumed that the phase errors have a certain correlation length, and the signal processing domain is shaped in a way that emphasizes the pairs of antenna positions separated by the distances not exceeding this correlation length. We want to mention two other facts about CINT imaging that are relevant to the current work:

- In its existing formulation, CINT has been used to address a different type of phase distortions, namely, the trajectory errors that can be described by setting $\xi = 1$ in (3).
- The output of CINT is a correlation image that has a good resolution w.r.t. the difference in the target coordinates but a significantly worse resolution in terms of the actual coordinates. Achieving full resolution in terms of the object coordinates in CINT imaging is still problematic [16, 17]. Hence, in its present form CINT cannot replace SAR, partially because the utility of CINT images remains limited.

Obtaining the elevation of a turbulent phase screen shall be considered an important first step toward the focusing of SAR images affected by transionospheric propagation. At this step, no detailed information about Ψ is required. On the contrary, once the value of ξ has been established, we can proceed to the reconstruction of the screen density function Ψ . An approach to the reconstruction of Ψ will be presented in our future work.

Other examples of reconstruction of the ionospheric parameters with the goal of reducing the image distortions can be found, e.g. in [3–6, 14, 19–25]. They may rely on the measurement of the Faraday rotation angle, use of the GPS signals, or co-registration of SAR images. To take advantage of Faraday rotation, polarimetric imaging may be required [2, 14, 22].

For airborne radar platforms, an important cause of image distortions is the air turbulence leading to the roughness of the platform trajectory. Autofocus procedures [26–30] have been developed to mitigate the effect of uncertainty in the platform position. The present formulation of CINT [15–18] aims at precisely this class of distortions.

The reconstruction of ionospheric parameters may also exploit the difference between two distortions of the signal phase for a pair of SAR images that realize the scenario of radar interferometry [31]. There are, in fact, different kinds of radar interferometry. The most popular one is the so-called cross-track interferometry, also known as InSAR, with the primary goal of generating digital elevation maps of the Earth's surface [1, 32, 33]. Two or more antenna signal acquisitions (or antenna tracks) are used in InSAR, and the methodology benefits from incorporating the data from multiple interferometric pairs as a way to mitigate the decorrelation and other sources of noise [34–37]. On the other hand, CINT is similar to along-track interferometry (see, e.g. [1, chapter IV] and [38, section 5.13]) where the data are taken from a single acquisition. In this work, we do not consider building CINT images from multiple antenna trajectories.

The rest of the article is organized as follows. Section 2 presents a brief overview of SAR imaging through a phase screen in a full-fledged 3D setting, as well as in a 2D formulation with only the cross-range image coordinate. The essentials of CINT imaging in their current

form are introduced in section 3. Section 4 presents our customization of CINT to the phase screen model and also highlights the differences between this case and the one of the trajectory errors. The main result of the study is presented in section 5 where we describe the procedure of vertical focusing, i.e. determination of the relative elevation of the phase screen using CINT imaging. We demonstrate this procedure numerically in section 6 and discuss the significance, limitations, and possible extensions of this work in section 7. Appendix A discusses technical details of the transition to the 2D formulation, and appendix B presents a short parameter study.

2. SAR imaging in the presence of a phase screen

2.1. Three-dimensional formulation

The most common interrogating waveform $P(t)$ used in radar imaging is a linear frequency-modulated chirp. The parameters of the chirp are its carrier frequency ω_0 , bandwidth B , and duration τ , so that

$$P(t) = \underbrace{\chi_\tau(t) \exp(-i\alpha t^2)}_{A(t)} \underbrace{\exp(-i\omega_0 t)}_{\text{carrier}}, \quad (4)$$

where $\alpha = \frac{B}{2\tau}$ is the chirp rate, and χ_τ is the characteristic function of the interval $[-\tau/2, \tau/2]$:

$$\chi_\tau(t) = \begin{cases} 1 & \text{if } |t| \leq \tau/2, \\ 0 & \text{otherwise.} \end{cases} \quad (5)$$

The wavelength λ that corresponds to the carrier frequency ω_0 is $\lambda = 2\pi c/\omega_0$. Typically $B \ll \omega_0$; in this case, $A(t)$ is called the pulse envelope [10].

The full geometry of SAR imaging through a phase screen is shown in figure 2. We assume that the signal propagates in free space, but its phase undergoes a jump when the ray crosses a certain plane called the phase screen. We assume that $\mathbf{z} = (\mathbf{z}, 0) \equiv (z_1, z_2, 0)$ are the target coordinates, $\mathbf{x} = (\mathbf{x}, H) \equiv (x_1, -L, H)$ are the antenna coordinates, and $\mathbf{s} = (s_1, s_2)$ are the two-dimensional coordinates on the phase screen, see figure 2. The ray is a straight line connecting the antenna and target locations, and the point where this line intersects the phase screen is $\mathbf{s}(x_1, \mathbf{z})$. The magnitude of the phase perturbation for the signal round trip will be denoted by $-\psi(x_1, \mathbf{z}) = -\Psi(\mathbf{s}(x_1, \mathbf{z}))$.⁴ The length of the synthetic aperture is denoted by L_{SA} , so that the synthetic aperture for the image coordinates $\mathbf{y} = (\mathbf{y}, 0) \equiv (y_1, y_2, 0)$ is defined as $\chi_{L_{\text{SA}}}(x_1 - y_1)$, see (5). For simplicity, we will also use $\chi_{L_{\text{SA}}}(x_1 - z_1)$ to denote the footprint of the antenna beam originating from the point \mathbf{x} at the antenna trajectory [4, 11].

The signal g received at \mathbf{x} is a superposition of radar pulses scattered off the target within the beam footprint:

$$g(x_1, t) \approx \int \chi_{L_{\text{SA}}}(x_1 - z_1) \nu(\mathbf{z}) P(t - 2R_z/c) \exp(-i\psi(x_1, \mathbf{z})) d\mathbf{z}, \quad (6)$$

where c is the speed of light, $R_z = |\mathbf{x} - \mathbf{z}|$, and $\nu(\mathbf{z})$ is the reflectivity of the target surface. While the source of phase perturbation is the dispersion, ψ does not depend on the frequency

⁴ Since the phase velocity of electromagnetic waves in the ionospheric plasma exceeds the speed of light [4, section 3.1], the transionospheric propagation leads to a phase advance. Accordingly, the sign at $\psi(x_1, \mathbf{z})$ coincides with that in the carrier part of (4). For this work, the choice of the sign is inconsequential. The actual phase jump for a ray crossing the phase screen at the point \mathbf{s} is $-\Psi(\mathbf{s})/2$ in either direction.

The phase screen formulation (6) and (8) is commonly used for modeling of the ionospheric turbulence in the context of SAR, see, e.g. [40, 41]. This model represents an ionosphere that has infinitesimal thickness. Accordingly, the point $(s, \xi H)$ is often called the ‘ionosphere piercing point’ (IPP, see, e.g. [3]) for the line connecting \mathbf{x} and \mathbf{z} , see figure 2. The case of $\xi = 0$ is degenerate because the resulting $\psi(x_1, \mathbf{z}) = \Psi(\mathbf{z})$ does not depend on x_1 , making it possible to merge the unknown phase perturbation in (6) with the complex phase of the unknown reflectivity function and redefine the latter as $\nu(\mathbf{z}) \exp(-i\Psi(\mathbf{z}))$.

The elevation of the ionospheric phase screen is often taken as the altitude where the maximum background electron number density is achieved, about 350 km above the Earth’s surface, in the F-layer of the ionosphere [3, 13]. Hence, for most low-orbit SAR satellites [1], the IPPs are approximately half-way between the antenna and the target: $\xi \sim 0.5$. In practice, the vertical profile of the electron number density in the ionosphere varies with time of the day, geographic location, solar cycle, ionospheric weather [12], etc. Moreover, the turbulent fluctuations of the electron number density that actually define the screen may be more prominent at a different altitude. Therefore, the main focus of this study is to build a procedure for determining ξ with the help of CINT imaging.

2.2. Two-dimensional formulation in dimensionless coordinates

The rationale behind the transition to the two-dimensional SAR formulation is the observation that imaging in range is less prone to phase distortions than imaging in azimuth, see [7] or [4, chapter 4]. The range resolution Δ_R of SAR is related to the signal bandwidth B as $\Delta_R = \pi c/B$ [1, 10, 11]. We can assume that both the imaged scene and the image consist of a number of range bins of width $\sim \Delta_R$, see figure 2. Using the procedure called range compression detailed in appendix A, we can reformulate the expression for the antenna signal in such a way that the contributions from different range bins separate. Then, the imaging geometry for each bin can be considered in a separate plane passing through this bin and the antenna trajectory, similar to figure 1. In particular, formula (1) can be used to express R_z and R_y in (6) and (7), respectively, via R defined for each bin separately.

We normalize the cross-range, i.e. azimuthal, coordinates using the azimuthal resolution $\Delta_A = \pi Rc/(\omega_0 L_{SA})$ (see [1, 10, 11]) as the nondimensionalization unit:

$$x_1 = x\Delta_A, \quad y_1 = y\Delta_A, \quad z_1 = z\Delta_A, \quad s_1 = s\Delta_A. \quad (9)$$

The dimensionless synthetic aperture F and perturbation scale ℓ are defined as follows:

$$F = \frac{L_{SA}}{\Delta_A} = \frac{L_{SA}^2 \omega_0}{\pi Rc} = \frac{2L_{SA}^2}{\lambda R} \gg 1, \quad \ell = \frac{\mathcal{L}}{\Delta_A}. \quad (10)$$

Since we are interested in the case where $\mathcal{L} \ll L_{SA}$, see section 2.1, we have $\ell \ll F$. The parameter F given by (10) is 8 times the Fresnel number as defined in [42, p 417]. It is equal to the ratio of the Fraunhofer distance of the synthetic array $\frac{2L_{SA}^2}{\lambda}$ to the propagation distance R , see [4, section 2.4], so that the target appears in the near field of the array.

Transition to the two-dimensional formulation (see appendix A) can be described as range compression for the signal $g(x_1, t)$ and removal of the fast phase on the Bragg wavelength from both the signal and the image [4, 43]. In dimensionless form, the equations for the new antenna signal $u(x)$ and new image $\mathcal{I}(y)$ obtained from (6) and (7) are as follows:

$$u(x) = \int \chi_F(x-z) \exp(i\pi(x-z)^2/F) \exp(-i\psi(x,z)) \mu(z) dz, \quad (11)$$

$$\mathcal{I}(y) = \int \chi_F(x-y) \exp(-i\pi(x-y)^2/F) \exp(i\psi_{\text{rec}}(x,y)) u(x) dx, \quad (12)$$

rel. noise level = 0.1, perturbation amplitude = 0.6
 $\xi_0 = 0.5, \xi = 0.58$

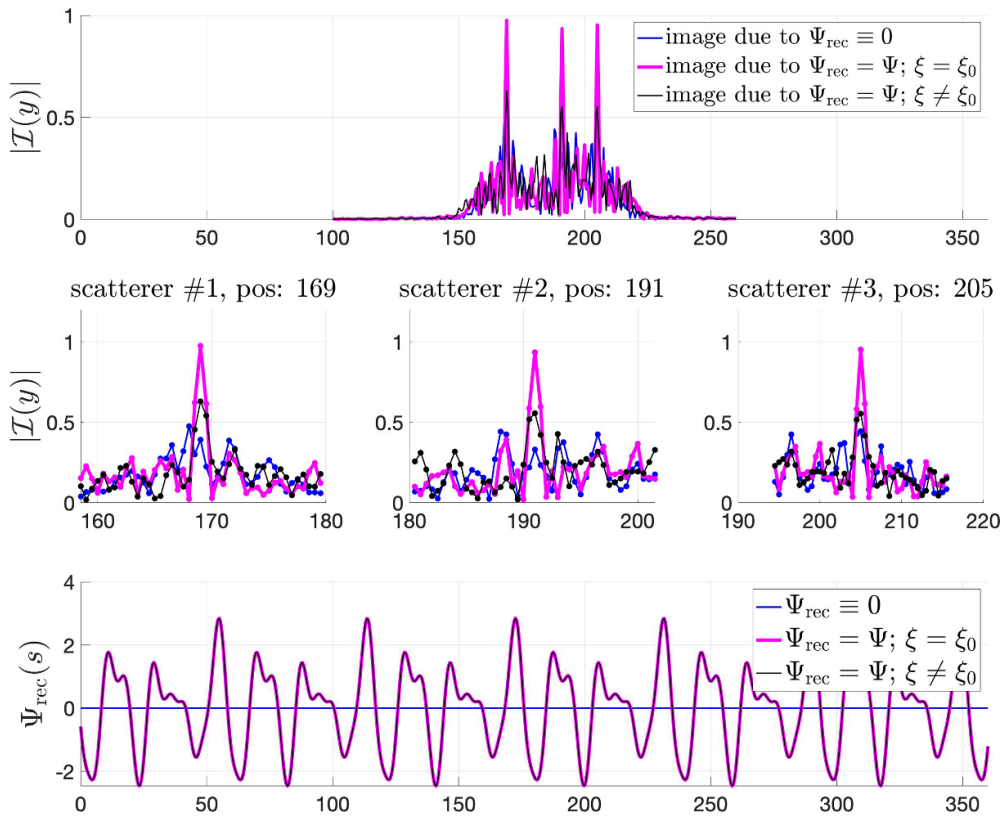


Figure 3. SAR imaging in the presence of a phase screen. Top: plots of image amplitude given by (12) for three choices of ψ_{rec} . Middle row: zoom-ins to the top plot around the locations of point scatterers, see (29). Bottom: the reconstructed screen density functions $\Psi_{\text{rec}}(s)$ used to build the above images.

where χ_F is defined according to (5). Accordingly, the phase screen model (8) becomes

$$\psi(x, z) = \Psi(s(x, z)), \quad \psi_{\text{rec}}(x, y) = \Psi_{\text{rec}}(s(x, y)), \quad \text{where } s(x, z) = \xi x + (1 - \xi)z. \quad (13)$$

For numerical simulations, we can also add noise to the data. When the coordinate x is discretized, we use x_j instead of x and define the noise component of the antenna signal by introducing the relative noise level p_{noise} and independent identically distributed standard Gaussian processes n_{re} and n_{im} :

$$n(x_j) = \frac{p_{\text{noise}}}{\sqrt{2}} \max_j |u(x_j)| \cdot (n_{\text{re}}(x_j) + in_{\text{im}}(x_j)). \quad (14)$$

Then, we define $u_{\text{noisy}}(x_j) = u(x_j) + n(x_j)$, where $u(x_j)$ is obtained by discretizing (11), and use u_{noisy} instead of u in the discretized version of (12).

2.3. Example: phase correction for SAR imaging

As a motivating example, figure 3 (top plot) shows the one-dimensional SAR images (12) obtained with and without compensation of phase distortions ($\Psi_{\text{rec}} = \Psi$ and $\Psi_{\text{rec}} \equiv 0$, respectively). For all these images, the target is represented by three point scatterers at the dimensionless coordinates 169, 191, and 205 (see more detail about the simulation parameters in section 6). The data $u_{\text{noisy}}(x)$ is obtained using (11) and (14) for the screen density $\Psi(s)$ shown in the bottom panel of figure 3 and $\xi = \xi_0 = 0.5$.

The point scatterers produce peaks in the SAR images shown in the top panel of figure 3 and also in the zoom-in clips in the middle row. We see that without compensation (blue curves), the level of phase perturbations is high enough to make the peaks undetectable. When in the reconstruction formula (12) we use the same phase screen density and elevation as in (11), the resulting peaks are narrow and high (purple curves). However, if the signal is built with $\xi_0 = 0.5$ whereas $\xi = 0.58$ is used for the reconstruction, then the peaks appear much lower and wider (black curves), which implies image degradation. Hence, it is important to accurately know the actual screen elevation at a time of image acquisition.

Of course, if Ψ were known, then it would be easy to take multiple values of ξ , build multiple SAR images using $\Psi_{\text{rec}} = \Psi$, and then select the value of ξ that yields the best image. However, it is more realistic to assume that neither Ψ nor ξ are known *a priori*.

In the rest of the paper, we address the problem of determining the value of ξ from the data without the knowledge of Ψ . We have chosen CINT as a tool because CINT images are stable with respect to disturbances [15] and, therefore, can be constructed using $\Psi_{\text{rec}} \equiv 0$, which is the easiest and always available option.

3. CINT imaging

The goal of CINT imaging is to increase the stability of the resulting image to random fluctuations of the signal phase. In order to present a rationale behind using the two-point CINT images [16, 17], it is convenient to take a pair of image coordinates (y_a, y_b) and express $\mathcal{I}(y_a)\mathcal{I}(y_b)$ as a double integral following (12):

$$\begin{aligned} \mathcal{I}(y_a)\overline{\mathcal{I}(y_b)} &= \iint \chi_F(x_a - y_a)\chi_F(x_b - y_b) \cdot \exp(-i\pi(x_a - y_a)^2/F) \\ &\quad \times \exp(i\pi(x_b - y_b)^2/F)u(x_a)\overline{u(x_b)}dx_a dx_b. \end{aligned} \quad (15)$$

In building $\mathcal{I}(y_a)$ and $\mathcal{I}(y_b)$ on the left hand side of (15), we consider the perturbation ψ unknown and, accordingly, take $\psi_{\text{rec}} \equiv 0$, so the terms in (12) that contain ψ_{rec} are not present on the right hand side.

Moreover, we assume in this section that the perturbation depends on the antenna position but not the target coordinate, i.e.

$$\psi(x, z) \equiv \Psi(x). \quad (16)$$

Expression (16) is an extreme case of (13) for $\xi = 1$. It associates the phase distortions with the trajectory coordinate alone and is equivalent to the most common case of SAR autofocus where the goal is to compensate for the trajectory errors.

Substituting (11) and (16) into (15), we obtain:

$$\begin{aligned} \mathcal{I}(y_a)\overline{\mathcal{I}(y_b)} &= \iiint \exp\left(\frac{i\pi}{F}(-(x_a - y_a)^2 + (x_a - z_a)^2 + (x_b - y_b)^2 - (x_b - z_b)^2)\right) \\ &\quad \cdot \chi_F(x_a - z_a)\chi_F(x_a - y_a)\chi_F(x_b - z_b)\chi_F(x_b - y_b) \\ &\quad \cdot \exp(i\Psi_b - i\Psi_a)\mu(z_a)\overline{\mu(z_b)} dx_a dx_b dz_a dz_b, \end{aligned} \quad (17)$$

where

$$\Psi_a = \psi(x_a), \quad \Psi_b = \psi(x_b). \quad (18)$$

The phase perturbation enters formula (17) via the exponential factors in its last line. These factors are due to (11) where they describe the inhomogeneity of the propagation medium. Unlike ψ_{rec} in (12), which is an attribute of the signal processing method, they cannot be arbitrarily removed.

The central idea of CINT imaging is to limit the effect of the perturbation by modifying the integration domain in (15). For example, if Ψ has a bounded derivative, then the effect of $\exp(i\Psi_b - i\Psi_a)$ in (17) can be limited by setting a bound on $|x_b - x_a|$:

$$|x_b - x_a| \leq l \implies |\Psi_b - \Psi_a| \approx \left| \Psi' \left(\frac{x_a + x_b}{2} \right) \right| \cdot |x_b - x_a| \leq \left| \Psi' \left(\frac{x_a + x_b}{2} \right) \right| \cdot l. \quad (19)$$

This can be implemented via adding one more characteristic function, $\chi_l(x_a - x_b)$, to the integrands of (15) and (17). The quantity l in (19) is the length of the CINT sub-aperture. As discussed around equation (31), choosing $l \lesssim \ell$ helps gain the stability w.r.t. perturbations.

Accordingly, we define the CINT image $Y(y_a, y_b)$ by modifying (15) as follows:

$$Y(y_a, y_b) = \iint_{(x_a, x_b) \in \mathcal{D}} \exp(-i\pi(x_a - y_a)^2/F) \exp(i\pi(x_b - y_b)^2/F) u(x_a)\overline{u(x_b)} dx_a dx_b, \quad (20)$$

where the signal processing domain \mathcal{D} is specified by

$$\mathcal{D} = \text{supp}_{(x_a, x_b)} (\chi_F(x_a - y_a)\chi_F(x_b - y_b) \cdot \chi_l(x_a - x_b)). \quad (21)$$

The geometry of the signal processing domains for (15) and (20) is illustrated in figure 4.

Formula (20) can be recast as follows:

$$Y(y_a, y_b) = \iint \mu(z_a)\overline{\mu(z_b)} K(y_a, y_b; z_a, z_b) dz_a dz_b, \quad (22)$$

where

$$\begin{aligned} K(y_a, y_b; z_a, z_b) &= \iint_{(x_a, x_b) \in \mathcal{D}} \chi_F(x_a - z_a)\chi_F(x_b - z_b) \exp(i\varphi_K) \\ &\quad \cdot \exp(i\Psi_b - i\Psi_a) dx_a dx_b \end{aligned} \quad (23)$$

is the CINT imaging kernel, and φ_K is the phase in the first line of (17).

Introduce the new variables:

$$\begin{aligned} x_M &= (x_a + x_b)/2, & x_D &= x_b - x_a, \\ y_M &= (y_a + y_b)/2, & y_D &= y_b - y_a, \\ z_M &= (z_a + z_b)/2, & z_D &= z_b - z_a. \end{aligned} \quad (24)$$

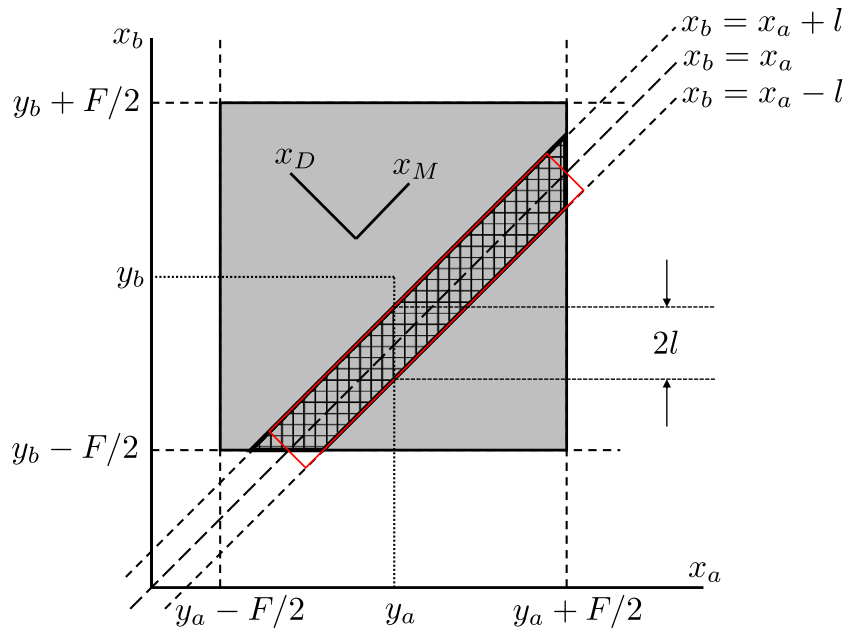


Figure 4. The signal processing domain, i.e. the domain of integration over (x_a, x_b) , for formulae (15) (shaded) and (20) (patterned). The red rectangle is the approximation (26) of the latter domain (the domain \mathcal{D} of (21)).

This allows us to simplify the expression for φ_K as follows:

$$\begin{aligned} \varphi_K &= \frac{\pi}{F} (-(x_a - y_a)^2 + (x_b - y_b)^2 + (x_a - z_a)^2 - (x_b - z_b)^2) \\ &= \frac{\pi}{F} (-2x_D(y_M - z_M) - 2x_M(y_D - z_D) + 2(y_D y_M - z_D z_M)). \end{aligned} \tag{25}$$

If the perturbation due to Ψ in (23) is so small that its effect is insignificant, then the integration with φ_K given by (25) can easily be performed by approximating \mathcal{D} with a long and narrow rectangle in the coordinates (x_M, x_D) , see figure 4:

$$-F'/2 \leq x_M - y_M \leq F'/2, \quad -l/2 \leq x_D \leq l/2, \tag{26}$$

where

$$F' = F - |y_D|. \tag{27}$$

This yields the unperturbed kernel:

$$\begin{aligned} K_0(y_a, y_b; z_a, z_b) &= K(y_a, y_b; z_a, z_b) \Big|_{\Psi=0} \\ &= lF' \operatorname{sinc}(\pi(y_M - z_M)l/F) \operatorname{sinc}(\pi(y_D - z_D)F'/F), \end{aligned} \tag{28}$$

see [17], where expression (28) is accurate to an inessential phase term. If we define the resolution as semi-width of the main lobe of a sinc kernel, then formula (28) implies that the resolution is high in terms of the coordinate difference y_D but poor with respect to the actual coordinate y_M (as $l \lesssim \ell$, we have $l \ll F$ according to (10)).

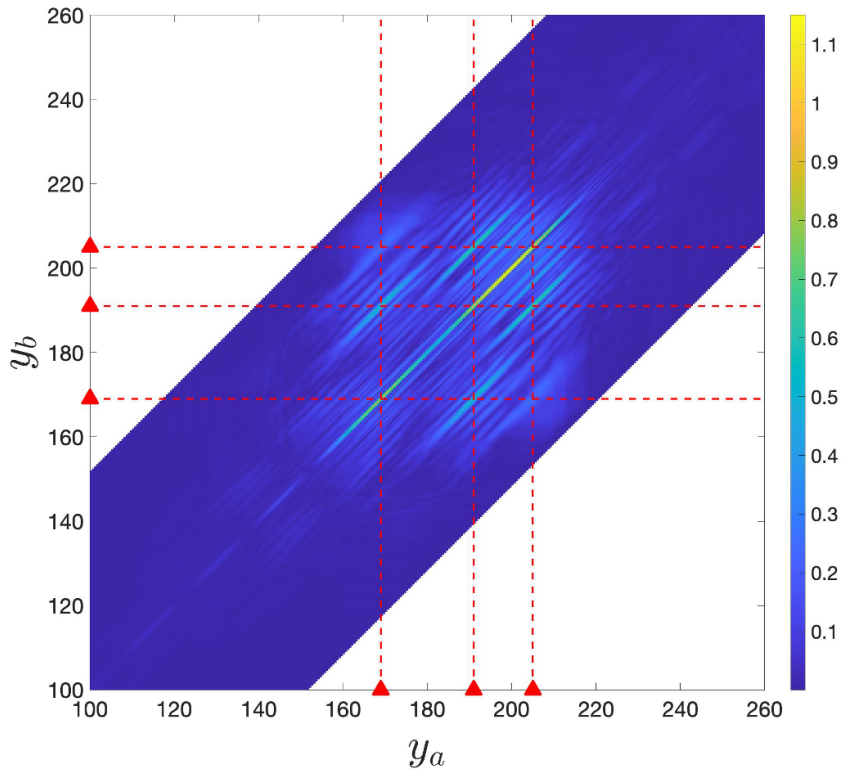


Figure 5. Plot of $|Y(y_a, y_b)|$, see (20) and (21) for $\Psi \equiv 0$. The red triangles and dashed lines indicate locations of the point scatterers, see (29). The streaks are centered at the intersections of the red dashed lines.

For the target, we use the model of isolated point scatterers:

$$\mu(z) = \sum_{\alpha \in \{a, b, \dots\}} \mu_\alpha \delta(z - z_\alpha^{\text{PS}}), \tag{29}$$

where z_α^{PS} and μ_α are constants and δ is the Dirac delta function. Then, formulae (22) and (28) yield the following expression for the unperturbed CINT image:

$$Y_0(y_a, y_b) = Y(y_a, y_b) \Big|_{\Psi=0} = lF' \sum_{\alpha, \beta \in \{a, b, \dots\}} \mu_\alpha \bar{\mu}_\beta \text{sinc}(\pi(z_\alpha^{\text{PS}} + z_\beta^{\text{PS}} - 2y_M)l/(2F)) \times \text{sinc}(\pi(z_\beta^{\text{PS}} - z_\alpha^{\text{PS}} - y_D)F'/F), \tag{30}$$

where y_M and y_D are defined in (24). In figure 5, each term in the sum on the right hand side of (30) produces a streak oriented along the y_M -axis that is narrow in the y_D -direction. A similar behavior can be observed in [17, formula (3.3) and figure 5.2] where the rectangular profile $\chi_l(x_a - x_b)$ in (21) is replaced with a Gaussian profile of width $\sim l$.

Returning to the original definition of Y in (20) with $\Psi \neq 0$, to reduce the effect of phase perturbations, it is suggested in [16, 17] to take l somewhat smaller than the correlation length of the perturbations ℓ : $l \lesssim \ell$, where it is assumed that the value of ℓ is known. It is shown that

the effect of the perturbations can be evaluated in terms of the variance and expectation of the CINT image:

$$\text{Var}[Y] = \mathcal{O}(l^2/\ell^2)\mathbb{E}[Y]^2, \quad (31)$$

see [16, equation (4.31)]. This indicates the statistical stability because $\text{Var}[Y]/\mathbb{E}[Y]^2$ vanishes as $l/\ell \rightarrow 0$, and Y approaches Y_0 given by (30). The physical intuition behind the reduced sensitivity to phase perturbations in this case is the cancellation of perturbation phases in (23) if x_a and x_b are close enough to consider $\Psi_a \approx \Psi_b$. In practice though, the value of l has a lower bound because the CINT sub-aperture should accommodate multiple antenna pulses, while the spacing between the antenna pulses is usually of the order of the resolution size due to the sampling and aliasing restrictions, see, e.g. [4, section 2.4.2] and [11, section 4.5.3]. Accordingly, we require $l \gg 1$ (recall that the azimuthal resolution Δ_A is chosen as the nondimensionalization unit in (9) and (10)). As (31) requires $l/\ell \lesssim 1$, we obtain the following double inequality:

$$1 \ll l, \ell \ll F. \quad (32)$$

Altogether, we see that the stability of a CINT image is achieved by adjusting the shape of the data processing domain to the correlation length of the perturbations, but the price to pay for this stability is a reduction of resolution in the absolute coordinate.

4. Adaptation of CINT to the phase screen model

This section presents the modifications necessary to adapt the CINT approach of [16, 17] to imaging through the phase screen.

Relation (19) is obtained under the assumption of $\xi = 1$, see (13) and (18), meaning that the phase perturbations occur at or near the antenna platform (e.g. are due to irregularities of the trajectory). In this case, the factor $\chi_l(x_a - x_b)$ in (21) is well suited to control the magnitude of distortions for all pairs (y_a, y_b) . However, when ξ is not very close to 1 and

$$|y_D| \approx |z_D| \gg l, \quad (33)$$

then condition $|x_a - x_b| \leq l$ is not optimal in terms of minimizing the distortions. Indeed, when $\xi \neq 1$, then $\Psi_b - \Psi_a = \Psi(x_b) - \Psi(x_a)$ in (23) is replaced with $\Psi(s_b) - \Psi(s_a)$. Accordingly, instead of $x_b - x_a$ in the estimate (19) we should use the screen coordinate as defined in (13):

$$s_b - s_a = \xi(x_b - x_a) + (1 - \xi)(z_b - z_a). \quad (34)$$

Hence, for $|y_D| \approx |z_D| = |z_b - z_a| \gg l$, the phase distortions in the integrand of (23) for $\xi \sim 0.5$ may appear much larger than those for $\xi = 1$, as illustrated in figure 6. Geometrically, this means that in the case where $\xi \sim 0.5$ and $|z_D| \gg l$, the sub-aperture gives rise to two clusters of IPPs, henceforth denoted as $\{s_a\}$ and $\{s_b\}$. The distance between these clusters is given by $(1 - \xi)|z_b - z_a|$, i.e. not controlled by l .⁵ Therefore, statistical stability should not be expected for such a configuration.

Yet we can restore control over the size of the domain of all IPPs, i.e. $\max |s_b - s_a|$, for $|z_b - z_a| \gg l$ by creating an offset x_O between the sub-apertures for x_a 's and x_b 's in the trajectory, as illustrated in figure 7. To do that, we redefine x_M and x_D as follows:

$$x_a = x_M - \frac{x_O}{2} - \frac{x_D}{2}, \quad x_b = x_M + \frac{x_O}{2} + \frac{x_D}{2}, \quad (35)$$

⁵ The two clusters actually separate when the first inequality in (38) does not hold.

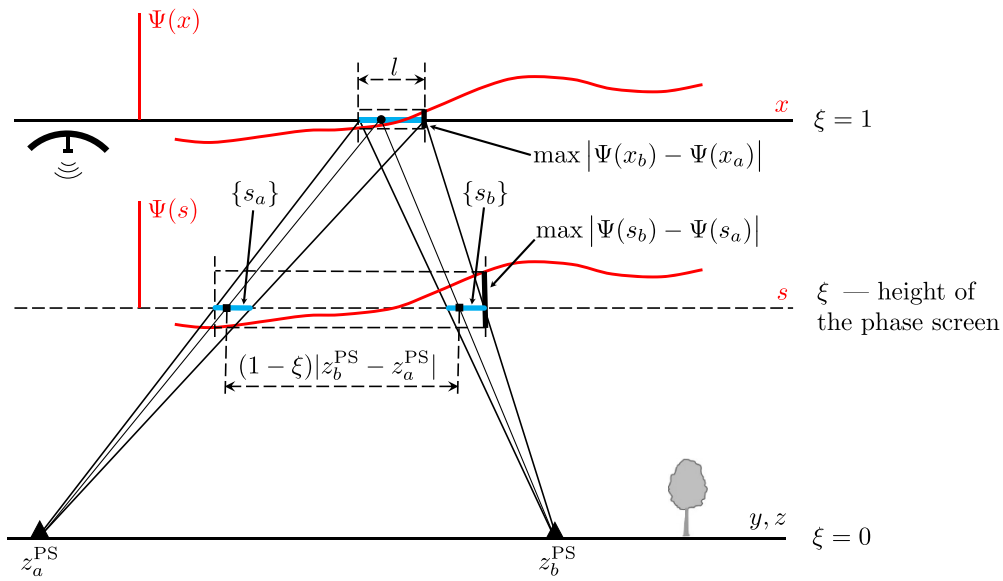


Figure 6. Geometry of CINT imaging according to formulation (21). The clusters $\{s_a\}$ and $\{s_b\}$ are shown in light blue; for $\xi = 1$ they overlap and coincide with the CINT sub-aperture, whereas for $\xi \sim 0.5$ they are disjoint. The black solid squares denote the IPPs for a specific antenna position x marked by a black dot. The red curves represent the phase perturbation functions $\Psi(x)$ and $\Psi(s)$. The thick black vertical bars illustrate the magnitude of the phase difference in the second line of (23) for $\xi = 1$ and $\xi \sim 0.5$.

whereas $y_M, y_D, z_M,$ and z_D are still defined by (24). We assume that x_0 is a constant determined by $(y_b - y_a)$ and ξ , while the interval of x_D is centered about zero as in the case of $\xi = 1$, see (26).

The value of x_0 can be determined as follows. Using (13) for the rays passing through an interval of length l at the relative elevation ξ , see figure 7, we obtain

$$s_a = \xi x_a + (1 - \xi)y_a, \quad s_b = \xi x_b + (1 - \xi)y_b, \tag{36}$$

so that

$$s_b - s_a = \xi x_0 + (1 - \xi)y_D + \xi x_D.$$

For a fixed interval of x_D , the value of $\max |s_b - s_a|$ is minimal when

$$x_0 = x_0(\xi) = -y_D(1 - \xi)/\xi. \tag{37}$$

This choice of x_0 makes the two IPP clusters, $\{s_a\}$ and $\{s_b\}$, coincide as shown in figure 7. Note that for $y_D = 0$, the optimal choice $x_0 = 0$ does not depend on ξ .

An alternative way of obtaining relation (37) is by considering the similar triangles FEC and ABC in figure 7:

$$\frac{|x_0|}{1 - \xi} = \frac{|y_b - y_a|}{\xi}.$$

Then, for geometrical reasons, the sign of x_0 as defined in (35) should be chosen opposite to that of $(y_b - y_a)$. The interval of x_D can also be found using similar triangles AFG and ACD in figure 7: $|x_D| \leq l/\xi$.

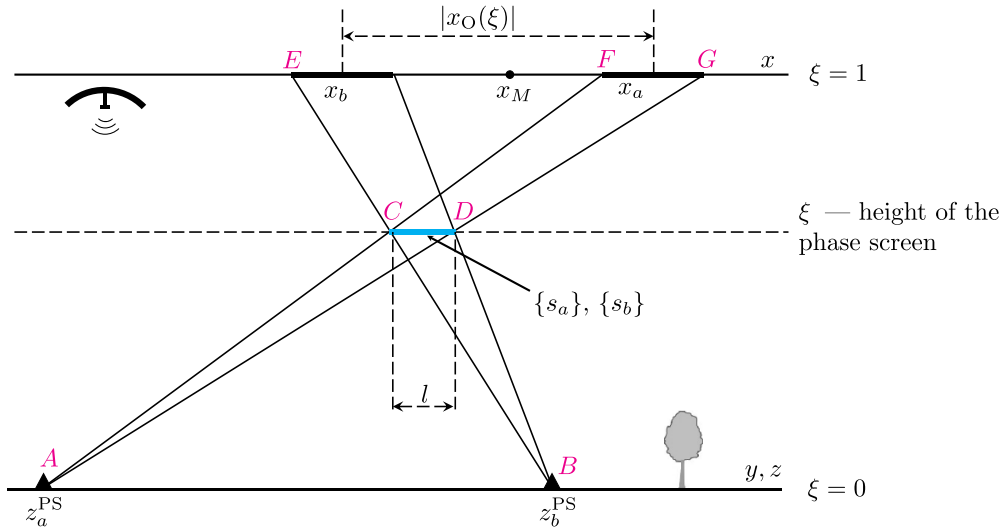


Figure 7. Geometry of CINT imaging through a phase screen according to formulation (39). Two thick segments of the antenna trajectory illustrate the separate sub-apertures for x_a and x_b . Introduction of an appropriate offset x_O between the sub-apertures for x_a and x_b makes subdomains $\{s_a\}$ and $\{s_b\}$ coincide, cf figure 6.

If condition (33) is satisfied and

$$(1 - \xi) < \frac{l}{|y_b - y_a|} \equiv \frac{l}{|y_D|} \ll 1 \tag{38}$$

(i.e. the phase screen is very close to the orbit), then $|x_O(\xi)| < l/\xi \approx l$. In this case, the introduction of x_O into (35) has little effect on $\max |\Psi(s_b) - \Psi(s_a)|$ because the sub-apertures for x_a and x_b overlap and $\max |s_b - s_a| \sim l$, unlike in the case of $\xi \sim 0.5$ shown in figure 6.

With the introduction of x_O , the imaging operator in (22) keeps its form, and the kernel $K(y_a, y_b; z_a, z_b)$ is still described by (23), but the new integration domain becomes:

$$\mathcal{D} = \text{supp}_{(x_a, x_b)} (\chi_F(x_a - y_a) \chi_F(x_b - y_b) \cdot \chi_l(x_b - x_a - x_O)). \tag{39}$$

This domain is illustrated in figure 8. Accurate to inessential phase terms, the expression for the unperturbed kernel K_0 resulting from (23) and (39) is given by (28) with (see (27))

$$F' = F - |y_D|/\xi. \tag{40}$$

Consider a pair of isolated point scatterers at $z = z_\alpha^{\text{PS}}$ and z_β^{PS} (see equation (29)) such that

$$l \ll |z_\alpha^{\text{PS}} - z_\beta^{\text{PS}}| \ll F. \tag{41}$$

It generates an off-diagonal streak in the CINT image, see figure 5. The second inequality in (41) means that when the perturbations are absent or low, this streak will be sharp, i.e. its width will be of the order of one. The latter can be seen from the second $\text{sinc}(\dots)$ on the right hand side in (30) because for $|y_D| \approx |z_\beta^{\text{PS}} - z_\alpha^{\text{PS}}| \ll F$ we have $F'/F \approx 1$, see (40). Then, given a sharp streak, we can measure the distance y_D^{streak} between this streak and the diagonal $y_a = y_b$ in figure 5 and thus approximate $(z_\beta^{\text{PS}} - z_\alpha^{\text{PS}})$ with high accuracy. The first inequality in (41) means that phase perturbations of sufficiently high amplitude can significantly deteriorate the streak if the data processing domain for the CINT image is chosen in the traditional way, i.e. as

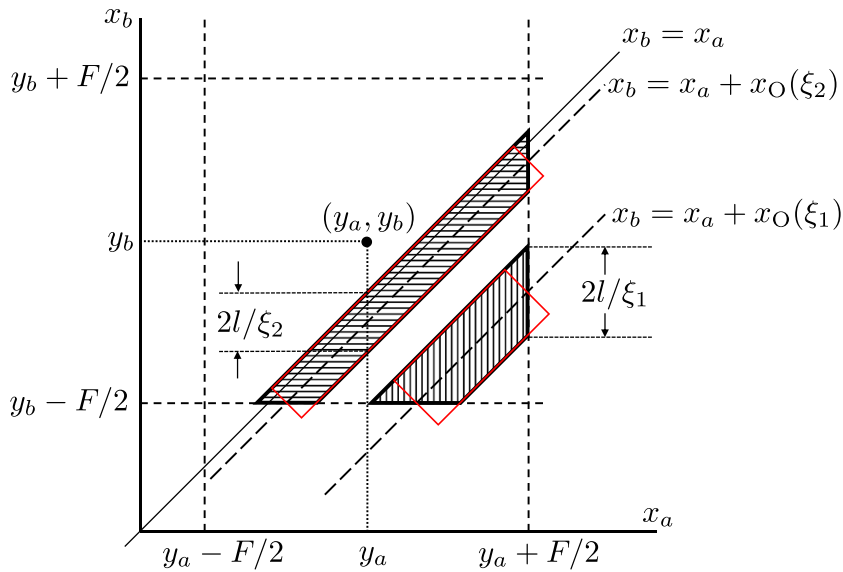


Figure 8. Two realizations of the domain (39) (see (21) and cf figure 4) for different values of ξ . The vertical pattern corresponds to $|1 - \xi_1| \sim 0.5$; in this case, the first inequality in (38) is violated, and an offset between the sub-apertures for x_a and x_b is necessary to merge the clusters $\{s_a\}$ and $\{s_b\}$, as in figure 7. The horizontal pattern corresponds to $1 - l/|y_b - y_a| < \xi_2 < 1$; this is the case where the inequalities in (38) are satisfied, so $\xi_2 \approx 1$, and these clusters overlap for $x_O = 0$, i.e. no offset is necessary.

in (21), see also figure 6. On the other hand, if we could obtain somehow a good estimate of $(z_\beta^{\text{PS}} - z_\alpha^{\text{PS}})$, then we can use its value in place of y_D in formula (37) to calculate x_O , substitute the latter into formula (39) for the modified data processing domain, and thus reduce this kind of distortion.

5. Vertical focusing of the CINT image

We exploit the anticipated dependence of the streak appearance on x_O formulated at the end of the previous section to build the following procedure for determining the unknown elevation of the phase screen provided that an estimate of $(z_\beta^{\text{PS}} - z_\alpha^{\text{PS}})$ is available.

Algorithm of vertical autofocus.

1. Choose an approximation ξ for the relative screen elevation using the available information, e.g. altitude of the orbit and that of the maximum mean electron number density in the ionosphere.
2. Build a CINT image using $x_O(\xi)$ and select an off-diagonal streak with $y_D^{\text{streak}} \approx z_\beta^{\text{PS}} - z_\alpha^{\text{PS}}$.
3. Seek the value of x_O that yields the clearest representation of this streak in the CINT image.
4. Retrieve the screen elevation ξ_0 from this x_O using (37).

In section 6, we will give the details of the numerical procedure, including the quantitative characterization for the ‘clarity of appearance’ of a streak in the CINT image. Note that a streak on the diagonal, i.e. the one due to $z_\alpha^{\text{PS}} = z_\beta^{\text{PS}}$, cannot be used in the above algorithm because,

as indicated after equation (37), for a diagonal streak $x_0 = 0$ is optimal and does not depend on ξ .

The foundation of the algorithm of vertical autofocus is the effect of phase distortions on the kernel K given by (23). In order to provide a quantitative characterization of this effect, we introduce:

$$\begin{aligned} \mathbb{E} \Psi &= \frac{1}{S} \int_s^{s+S} \Psi(s') \, ds', \\ \text{Var} \Psi &= \frac{1}{S} \int_s^{s+S} (\Psi(s') - \mathbb{E} \Psi)^2 \, ds', \\ \|\Psi'\|^2 &= \frac{1}{S} \int_s^{s+S} |\Psi'(s')|^2 \, ds', \\ \Delta_{ab} \Psi(s_M, s_D) &= \Psi_b - \Psi_a \equiv \Psi(s_b) - \Psi(s_a), \\ \|\Delta_{ab} \Psi(s_D)\|^2 &= \frac{1}{S} \int_s^{s+S} |\Delta_{ab} \Psi(s', s_D)|^2 \, ds', \end{aligned} \tag{42}$$

where $s_M = (s_a + s_b)/2$, $s_D = s_b - s_a$. Ψ' in the third equation of (42) is the derivative of Ψ , as in (19). As long as S satisfies $\ell \ll S \lesssim F$, the integrals in (42) are weakly affected by the choice of s . Then, the quantities (42) help us derive the following classification.

(A) The scale of variation of the perturbation phase:

$$\underbrace{\text{Var} \Psi \ll 1}_{\text{condition A1}} \quad \text{vs.} \quad \underbrace{\text{Var} \Psi \sim 1 \quad \text{or} \quad \text{Var} \Psi \gg 1}_{\text{condition A2}}.$$

When this scale is small (condition A1), the phase perturbations in the integral (23) average out, similarly to the case of SAR imaging considered in [5, 7, 39]. Hence, the resulting kernel K is close to K_0 given by (28) regardless of the choice of x_0 . Then, on one hand, the focusing procedure is not required because the perturbations can be ignored. On the other hand, it would not yield a reliable outcome anyway, because the unperturbed kernel K_0 is only weakly affected by the choice of x_0 , as stated at the end of section 4. Hence, we will be assuming hereafter that condition A2 holds, which is opposite to condition A1.

(B) The length of the sub-aperture vs. slope of the phase screen density:

$$\underbrace{\|\Psi'\| \cdot l \ll 1 \quad \text{or} \quad \|\Psi'\| \cdot l \sim 1}_{\text{condition B1}} \quad \text{vs.} \quad \underbrace{\|\Psi'\| \cdot l \gg 1}_{\text{condition B2}}.$$

Since we intend to preserve the main characteristics of the CINT approach, we always take $l \lesssim \ell$, see (31). Then, similar to (19), we can use $\Delta_{ab} \Psi(s_M, s_D) \approx \Psi'(s_M) \cdot s_D$, whereas $\max |s_D| \geq l$. Hence, under condition B2 with $|s_D| \sim l$, we have $\|\Delta_{ab} \Psi(s_D)\| \gg 1$. Consider $K(y_a, y_b; z_a, z_b) \equiv K(y_M, y_D; z_M, z_D)$ given by (23)–(27):

$$K(y_M, y_D; z_M, z_D) = \int_{y_M - F'/2}^{y_M + F'/2} \left(\int_{-l/2}^{l/2} \exp(i\varphi_K) \exp(i\Delta_{ab} \Psi) \, dx_D \right) dx_M.$$

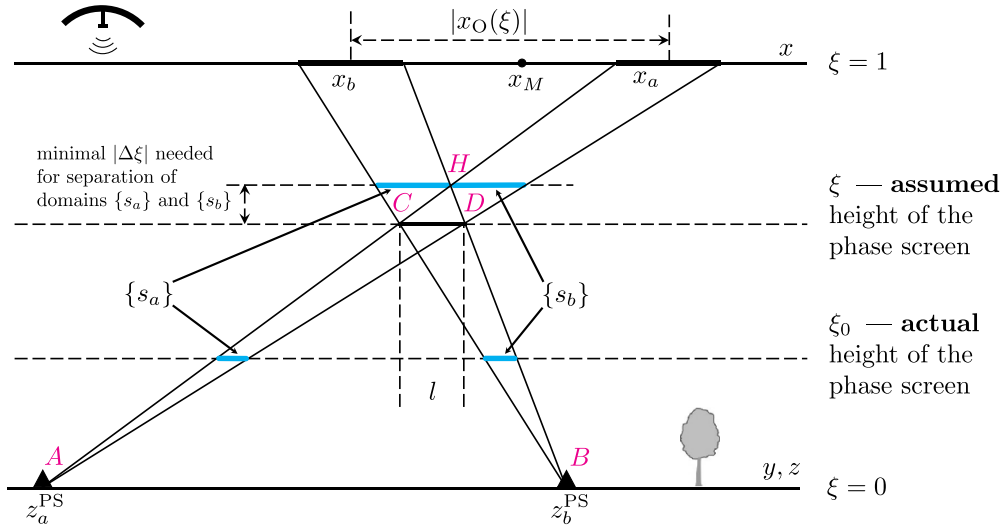


Figure 9. Geometry of CINT imaging through a phase screen in the case where the elevation of the screen is not known exactly. With x_O calculated according to (37), subdomains $\{s_a\}$ and $\{s_b\}$ may still be separated due to the difference between the assumed (ξ) and actual (ξ_0) phase screen elevation, cf figure 7.

Dropping the small exponent $(y_D - z_D)(1 - \xi)\Psi'(s_M)$, we rewrite it as

$$K(y_M, y_D; z_M, z_D) = \int_{-l/2}^{l/2} \exp\left(-\frac{2\pi i}{F} x_D (y_M - z_M)\right) \left(\int_{y_M - F'/2}^{y_M + F'/2} \exp\left(-\frac{2\pi i}{F} x_M (y_D - z_D)\right) \times \exp(i\xi x_D \Psi'[\xi x_M + (1 - \xi)z_M]) dx_M \right) dx_D. \quad (43)$$

Taking into account $l \ll F'$, we can see that if $\xi|x_D| \sim l$ then for the integral over dx_M , the term $\xi x_D \Psi'[\xi x_M + \dots]$ in the last exponent of (43) realizes many large-amplitude (as compared to 1) random oscillations of the complex phase over the interval of integration. As a consequence, this integral yields a speckle pattern w.r.t. $(y_D - z_D)$, see [7, 39]. Thus, even with the right choice of x_O , there will be no clear appearance of the streak and the suggested focusing procedure will not work. We will avoid this case and assume from here on that condition B1 is satisfied.

Let us denote the true (and unknown to the system) dimensionless elevation of the phase screen by ξ_0 , while its assumed value ξ (e.g. the initial guess) enters the signal processing procedure via (37) and (39). In the case where conditions A2 and B1 hold simultaneously, the relation between the screen elevation error $\Delta\xi = \xi - \xi_0$ and phase distortions can be described as follows:

- The phase distortions in the integral in (23) are large when ξ and ξ_0 (and, hence, the two domains of IPPs, $\{s_a\}$ and $\{s_b\}$, see figure 9) are far apart.

- The phase distortions are small or moderate when the values of ξ and ξ_0 are close (or, equivalently, $|\Delta\xi|$ is small) such that the domains $\{s_a\}$ and $\{s_b\}$ overlap.

We would like to characterize the scale for $\Delta\xi$ at which the distortions increase significantly w.r.t. the baseline case of $\Delta\xi = 0$. To do so, we will employ the criterion of geometric separation between the domains $\{s_a\}$ and $\{s_b\}$. Recall that while ξ_0 is unknown, we can control the value of ξ by modifying x_0 , see (37). By considering similar triangles CHD and AHB in figure 9, assuming that $\Delta\xi$ is small, and taking into account $|z_D| \gg l$, see (41), we present this criterion as

$$\frac{|\Delta\xi|}{l} > \frac{\xi_0}{|z_D|}, \quad \text{where} \quad \Delta\xi = \xi - \xi_0. \quad (44)$$

Note that for $\xi_0 = 1$, (44) is consistent with the first inequality in (38). We use the inequality in (44) to introduce the following parameter:

$$Q = \frac{(z_\beta^{\text{PS}} - z_\alpha^{\text{PS}}) \Delta\xi}{l \xi_0}. \quad (45)$$

When $|Q|$ exceeds 1, the phase distortions in the integral (23) may become much larger than those for the case of $Q = 0$ (i.e. $\Delta\xi = 0$), and this should manifest itself in the appearance of the corresponding off-diagonal streak in figure 5. Note that since $|z_\beta^{\text{PS}} - z_\alpha^{\text{PS}}|/l \approx |y_D|/l \gg 1$, this transition occurs at small values of $|\Delta\xi|/\xi_0$, making the proposed autofocus approach meaningful.

6. Numerical examples

In section 5, it has been determined that the case of $\xi = \xi_0$ (i.e. when the values of the assumed and actual screen elevations coincide) yields the clearest representation of off-diagonal streaks in the CINT image. The algorithm of vertical focusing on page 16 describes how this property of CINT images can be used to reconstruct the screen elevation from the radar data. In this section, we demonstrate vertical focusing in a numerical simulation. The simulation workflow is as follows.

1. One-dimensional reflectivity $\mu(z)$ and phase screen density $\Psi(s)$ functions, as well as the relative phase screen elevation ξ_0 , are defined as explained below.
2. The antenna signal $u(x_j)$ is calculated using a discretized version of (11).
3. The noise is added to $u(x_j)$ according to (14) resulting in $u_{\text{noisy}}(x_j)$.
4. A range of test values for ξ is chosen, a certain value of y_D is assumed.
5. For each value of ξ , the value of the offset parameter x_0 is calculated using (37).
6. For each value of x_0 , the signal processing domain \mathcal{D} is defined from (39).
7. For each domain \mathcal{D} , the noisy signal $u_{\text{noisy}}(x_j)$ is used instead of $u(x)$ in the discretized version of (20) yielding a discrete CINT image Y .
8. The characteristics of an off-diagonal streak (see figure 5) in the resulting CINT images are calculated, and the value of ξ is evaluated as described further in this section.

In practice, the initial value of y_D on step 4 can be defined using some *a priori* knowledge about the target, e.g. the available imagery. This value can be refined after step 7, such that steps 5–7 can be repeated with the updated value of y_D .

Table 1. Default parameters of numerical simulations. The simulation steps refer to the workflow on page 19.

Notation	Value	Workflow steps	Comment
F	100	2, 7	Equations (10)–(12).
grid step in x	0.5	2, 7	Equations (9)–(12).
grid step in y	0.5	7	Equations (9), (10), (12).
grid step in z	0.5	2	Equations (9)–(11).
ξ	multiple	5	Equation (13), figures 6 and 7.
ξ_0	0.5	2	Figure 9, section 5.
p_{noise}	0.1	3	Equation (14).
l	3	6	Equations (19), (21), Figures 4, 7, and 9.

Table 2. Default coefficients in formula (46) for Ψ , see step 1 in the workflow on page 19.

k_n	a_n	p_n	q_n
0.32044	0.79698	−0.14362	−0.78393
0.42726	0.44830	0.17568	−0.41244
0.53407	0.28691	−0.24331	−0.15206
0.64088	0.19925	0.14747	−0.13398
0.74770	0.14638	−0.05816	0.13433
0.85451	0.11208	−0.10357	−0.04282
0.96133	0.08855	−0.08308	0.03064

The default values for the main parameters of the simulations are presented in table 1. They realize a regime of very high distortions, as we will explain shortly. Besides, simulations for the values other than those in table 1 are described in appendix B.

For step 1 in the workflow above, the locations of the point scatterers in (29) are $z_a^{\text{PS}} = 169$, $z_b^{\text{PS}} = 191$, $z_c^{\text{PS}} = 205$, similarly to figure 3, and the streak for the vertical focusing procedure (step 8) is always due to the pair $(z_a^{\text{PS}}, z_b^{\text{PS}})$, see (30). The ionospheric screen density function $\Psi(s)$, see (13), is defined at step 1 as follows:

$$\begin{aligned}\Psi(s) &= \pi a_{\text{scr}} \cdot \text{Re} \sum_n a_n \exp(i k_n s + i \varphi_n) \\ &= \pi a_{\text{scr}} \sum_n (p_n \cos(k_n s) + q_n \sin(k_n s)),\end{aligned}\tag{46}$$

where we assume

$$\sum_n a_n^2 = \sum_n (p_n^2 + q_n^2) = 1.$$

The parameter a_{scr} is called the perturbation amplitude; its default value is 0.6, whereas the amplitudes a_n realize the amplitude spectrum $a_n \propto k_n^{-2}$. It is common to consider the complex phases φ_n in (46) as i.i.d. random variables with uniform distribution over $(0, 2\pi)$. A particular realization of $\{\varphi_n\}$, called the default realization, leads to the values of $p_n = a_n \cos \varphi_n$ and $q_n = -a_n \sin \varphi_n$, thus defining $\Psi(s)$. The values of k_n , a_n , p_n , and q_n for the default realization are listed in table 2. Three other realizations of $\Psi(s)$ are considered in appendix B, see table 3.

For the quantities in section 5 that define the classification according to items (A) and (B) on page 17, we have

$$\begin{aligned} \text{Var } \Psi &\sim \pi^2 a_{\text{scr}}^2 \cdot \frac{1}{2} \sum_n a_n^2 = \frac{\pi^2 a_{\text{scr}}^2}{2} \approx 1.78, \\ l \|\Psi'\| &\sim l \pi a_{\text{scr}} \cdot \left(\frac{1}{2} \sum_n k_n^2 a_n^2 \right)^{1/2} \approx 1.65. \end{aligned} \quad (47)$$

The correlation length ℓ is not used explicitly in representation (46). We note however that the period of the shortest harmonic, see table 2, is still approximately 2 times larger than the value of l in table 1, so that we assume that the parameter l^2/ℓ^2 in (31) is less than 1.

For the wavelength of the longest simulated harmonic, $\lambda_{\text{max}} = 2\pi/k_{\text{min}}$ in table 2, we have $F/\lambda_{\text{max}} \approx 5$, so this is a case of mid-scale perturbations that have the strongest effect on the image, see section 2.1. Taking into account that the perturbation amplitude exceeds one, see (47), it is not surprising to see that the SAR image is strongly affected by these perturbations, see the blue curves in figure 3. Note that for the Earth's ionosphere, the maximum expectation of the fluctuation magnitude may reach one, see [4, table 1.2], but since the turbulence is stochastic, we may encounter realizations with even higher level of perturbations. Altogether, the simulated screen density function realizes what can be seen as an extreme scenario of ionospheric distortions.

In order to demonstrate the defocusing effect of the screen elevation error on the CINT image, the left panels in figure 10 present the plots of $|Y(y_a, y_b)|$ in a neighborhood of $(y_a, y_b) = (z_a^{\text{PS}}, z_b^{\text{PS}})$ (cf figure 5) for several values of ξ . We see that as ξ approaches the true value of $\xi_0 = 0.5$, the streak at the center of the plot becomes sharper despite the absence of the phase correction. In order to quantify this effect, we specify certain intervals of y_M and y_D around $(y_a + y_b)/2$ and $(y_b - y_a)$, respectively. This defines a small red diamond in the plot. Then we collapse it into an interval by averaging $|Y|$ over y_M and plot the result as a function $\mathcal{Y} = \mathcal{Y}(y_D; \xi)$ in the respective right panels in figure 10. Notice that for $\mathcal{Y}(y_D; \xi_0)$, we obtain a sinc-like profile as predicted by (28), whereas for $\xi \neq \xi_0$ this profile is distorted.

Further, we define the 'peakedness' \mathcal{P} of the aforementioned profile as follows:

$$\mathcal{P}(\xi) = \int_{y_D \in \text{central peak}} \mathcal{Y}^2(y_D; \xi) dy_D \cdot \left(\int_{y_D \in \text{largest neighboring sidelobe}} \mathcal{Y}^2(y_D; \xi) dy_D \right)^{-1}, \quad (48)$$

where to identify the central peak and sidelobes, we use zeros of the second sinc in (28). We expect the peakedness to be at its maximum in the vicinity of $\xi = \xi_0$, and our numerical experiments confirm this hypothesis.

The use of \mathcal{P} in the vertical focusing procedure is demonstrated in figure 11. The left plots in this figure display the profiles $\mathcal{Y}(y_D; \xi)$ for several values of ξ . We make sure that none of the sampled values of ξ 'accidentally' hits the true value ξ_0 . The plots of $\mathcal{P}(\xi)$ obtained from these profiles are shown on the right. We can see that the arguments of the largest values of \mathcal{P} concentrate around ξ_0 . The procedure of finding the highest value of \mathcal{P} can be called focusing because \mathcal{P} characterizes the sharpness of the image. In the plots of $\mathcal{P}(\xi)$ in figure 11, the abscissa scales are adjusted depending on the value of l so as to make sure that the ranges of Q , see (45), are the same. Thus, we can observe that the deterioration of the streak profile can be related to the value of $|Q|$.

While the search for the maximum of a function of one variable, $\mathcal{P}(\xi)$, may seem trivial, each calculation of the function is numerically intensive, and the function itself is not necessarily convex. Hence, instead of using iterations to approach ξ_0 , we increase the robustness

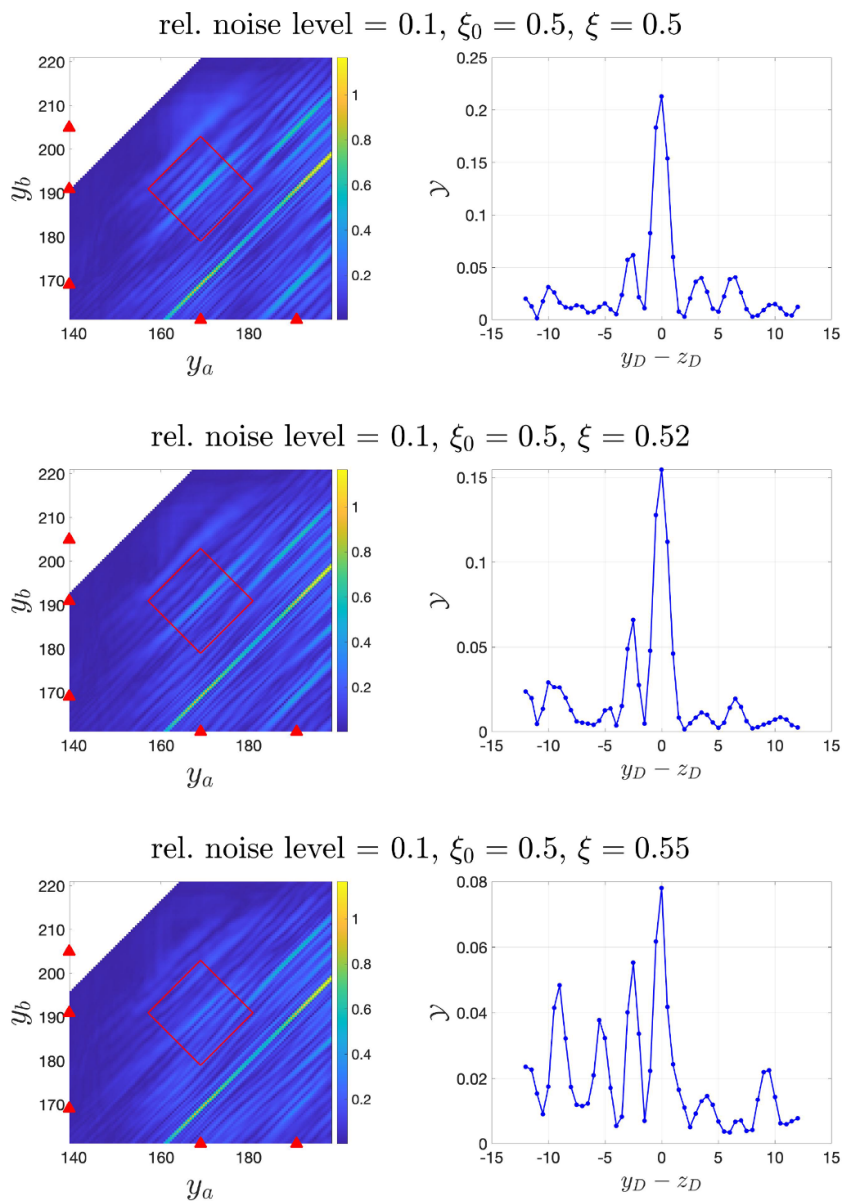


Figure 10. Effect of the difference between the actual screen elevation ξ_0 and assumed screen elevation ξ on the profile of a streak in the CINT image.

of finding the maximum by taking the five largest values of $\mathcal{P}(\xi)$, approximating them with a quadratic function, and taking the maximum of the latter. In our simulations, the result usually lies within 5% of the true value ξ_0 .

In appendix B, we explore how the foregoing focusing procedure may be affected by a variation of certain problem parameters. These parameters are as follows.

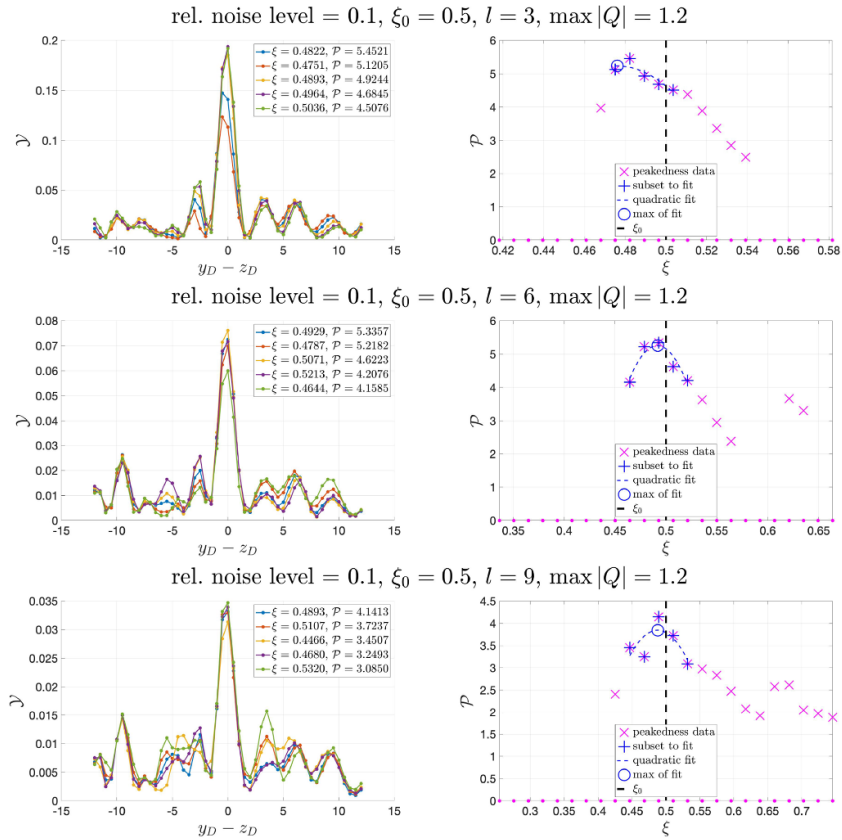


Figure 11. Determination of the phase screen height for several values of the CINT subaperture: $l = 3$ (top), $l = 6$ (middle), and $l = 9$ (bottom). The left panels plot $\mathcal{Y}(y_D; \xi)$ for the five largest values of \mathcal{P} on the right panel. The purple dots on the abscissa axis of the right panel indicate the values of ξ for which \mathcal{Y} has been calculated. Note that for some of these dots (i.e. for the corresponding values of ξ), no value of \mathcal{P} is given. These missing values of \mathcal{P} indicate the cases where \mathcal{Y} has no dominant peak at $y_D - (z_b^{\text{PS}} - z_a^{\text{PS}}) = 0$, e.g. the streak at the center of the diamond-shaped fragment in figure 10 cannot be detected or unambiguously identified, as is the case for the bottom row in figure 10, so formula (48) cannot be used.

- Realization of the set of complex phases φ_n in the Fourier representation of the phase screen density function (46) for the given values of a_{scr} , k_n , and a_n , see table 3 and figure 12.
- The perturbation amplitude a_{scr} in (46), see figure 13.
- The discretization steps for the calculation of quadratures in (11), (20), and (48), see figure 14.
- The noise level p_{noise} in (14), see figure 15.
- The distance between the scatterers $|z_a^{\text{PS}} - z_b^{\text{PS}}|$ determining the ‘focusing streak’, see formula (30) and figures 5 and 16.

7. Discussion and future work

We have introduced and implemented an approach for vertical focusing that allows us to derive the elevation of a phase screen from CINT images. In turn, having determined this parameter one can use it to reconstruct the phase screen density function that is needed to implement the correction of phase distortions in (12) [3].

The phase screen model that our development is focused on is widely used. Yet it can be seen as oversimplified when the actual ionosphere is considered. An extension of this model can be built by replacing the phase screen with a factorized form of the electron density:

$$\begin{array}{ccc} \psi(\xi, s) = \delta(\xi - \xi_0)\Psi(s) & \longrightarrow & \psi(\xi, s) = \psi_\xi(\xi)\Psi(s). \\ \text{(phase screen)} & & \text{(factorized model)} \end{array} \quad (49)$$

The factorized model (49) incorporates a wider class of vertical profiles of the electron density. It will be studied in the future.

In addition to using the phase screen for modeling of a three-dimensional ionosphere, the current work makes another simplifying assumption by requiring the presence of two separate point scatterers in a single range bin of the SAR image. This is not unlikely for imaging of urban scenes but may be problematic in other cases. Despite the above limitations, there are several reasons to study and use this setup. First, the phase screen model is very popular, so learning its properties is useful. Second, our model permits a simple geometric interpretation (see, e.g. figure 9) and some analytic predictions. Finally, this approach inherits the benefits of CINT, such as the simplicity (all formulations are explicit and there is no iterative procedure involved) and stability w.r.t. additive noise. According to the authors' knowledge, this work is the first demonstration of the possibility to use CINT for recovering the characteristics of inhomogeneities of the propagation medium.

The algorithm described in this work requires the presence of two isolated point scatterers in a single range bin. This strong requirement may be relaxed by performing a full-fledged three-dimensional simulation where it might be even reasonable to use multiple pairs of point scatterers to increase the robustness. A three-dimensional setup will also give us an opportunity to investigate the case where one or both of the point scatterers are located slightly off the plane illustrated in figure 7.⁶ Note that this kind of extension requires that the two-dimensional signal $g(x_1, t)$ given by (6) is used as the data, yielding a four-dimensional CINT image $Y(\mathbf{y}_a, \mathbf{y}_b)$. At this time, the authors have no estimates for the associated increase of the computational cost, including the search for a 'focusing streak', see (30) and figure 5, in a four-dimensional space $(\mathbf{y}_a, \mathbf{y}_b)$.

The procedure developed in this work is designed to deal with the small-scale (i.e. $\ell \ll F$) phase disturbances that originate from the ionospheric turbulence and cause the most significant problems to the ionosphere reconstruction procedures [4, 13, 22, 26]. Whereas for modeling of the ionosphere, the phase screen is typically located at the maximum of the vertical distribution of the electron density, the result of our vertical focusing may rather correspond to the effective height at which the medium is most turbulent. The implications of this effect require further study.

⁶ Generating and processing SAR data $u(\dots)$ for a three-dimensional problem in the two-dimensional setup may amount to a mild form of 'inverse crime' [44, section 5.3]; the latter refers to the parametrization of an inverse problem in such a way that the resulting finite-dimensional set of equations permits an exact solution. Arguably, the exact reconstruction is not likely in our case because the data (i.e. the antenna signal) contains noise, see (14).

Finally, we note that in SAR interferometry [31–33, 38], some averaging of the interferometric data is usually required. The latter is justified by a certain statistical model of the target. For example, in [45] an incoherent model of a source has been assumed, the coherence function of the data is exploited, and the source intensity is reconstructed. On the other hand, the current work relies on a deterministic (rather than stochastic) model of point scatterers, similarly to many other works that discuss autofocus [26]. For a stochastic model of the target, e.g. the speckle model [46]

$$\langle \nu(z_a) \overline{\nu(z_b)} \rangle = \sigma^2 \delta(z_a - z_b),$$

exploring the statistical properties of the CINT image may be of interest, given the high resolution of the latter in y_D due to the kernel (28). However, as formulated, this problem is beyond the scope of the current work.

Data availability statement

No new data were created or analysed in this study.

Acknowledgment

This work was supported by US AFOSR under Grant # FA9550-21-1-0086.

Appendix A. Two-dimensional formulation for the SAR imaging

A.1. Range compression

While the full-fledged three-dimensional formulation of SAR imaging is given in section 2.1, the main result of this work is presented in the two-dimensional formulation starting section 2.2. The main step in the transition is range compression. We find it convenient to introduce the corresponding framework using the context of SAR autofocus, in part because the autofocus procedures often operate with the range-compressed signal for actual determination and application of the phase correction term.

We can consider autofocus (see, e.g. [26]) as a three-stage process that replaces (7). At the first stage, the range compression is applied to the received signal (6) for each antenna position. The kernel of this transformation is

$$P^{\text{rc}}(d, t) = \overline{P(t - 2d/c)}, \quad (50)$$

where d is the focusing parameter, or range, related to the image coordinate by $d = R + y_2 L/R$, see figure 2. The resulting range-compressed signal is given by

$$g^{\text{rc}}(x_1, y_2) = \int P^{\text{rc}}(R + y_2 L/R, t) g(x_1, t) dt. \quad (51)$$

We emphasize that the first argument of P^{rc} in (51) is the distance taken purely along the range direction. In formula (6) though, $R_z = |\mathbf{x} - \mathbf{z}|$ is the distance between the two points for which, generally speaking, $x_1 \neq z_1$. Therefore, we employ the paraxial approximation⁷:

$$|\mathbf{x} - \mathbf{z}| \approx R + \frac{L}{R} z_2 + \frac{(x_1 - z_1)^2}{2R}, \quad (52)$$

⁷ To use the paraxial approximation in (7), one would also need a formula similar to (52) for the distance $|\mathbf{x} - \mathbf{y}|$. This, however, is not what's done in (51), where only the first two terms are retained: $d = R + y_2 L/R$.

cf (1). Introducing $k_{\parallel} = \omega_0 L / (cR)$ and $\psi(x_1, z_1, z_2) \equiv \psi(x_1, \mathbf{z})$, substituting (6) and (52) into (51), and integrating over t , we get:

$$g^{\text{rc}}(x_1, y_2) = \tau \exp(-2ik_{\parallel}y_2) \iint \chi_{L_{\text{SA}}}(x_1 - z_1) \exp(-i\psi(x_1, \mathbf{z})) \exp(i\omega_0(x_1 - z_1)^2 / (Rc)) \cdot \nu(\mathbf{z}) \exp(2ik_{\parallel}z_2) \text{sinc} \left[\frac{B}{c} \left((y_2 - z_2) \frac{L}{R} - \frac{(x_1 - z_1)^2}{2R} \right) \right] dz_1 dz_2. \quad (53)$$

The sinc function in (53) is defined as $\text{sinc} \zeta = (\sin \zeta) / \zeta$. The semi-width of its main lobe in the range variable d is given by

$$\Delta_R = \pi c / B. \quad (54)$$

This scale is called the range resolution and can be used to define a range bin of width $\Delta_R R / L$ centered at y_2 on the target plane, see figure 2. We assume that the function $\psi(x_1, z_1, z_2)$ varies slowly if we fix x_1 and z_1 and let z_2 vary within the bin. This will allow us to replace z_2 with y_2 in the argument of ψ . We also define two more slow functions of y_2 as follows:

$$\begin{aligned} u(x_1, y_2) &= g^{\text{rc}}(x_1, y_2) \exp(2ik_{\parallel}y_2), \\ \mu(z_1, y_2) &= \int \nu(\mathbf{z}) \exp(2ik_{\parallel}z_2) \text{sinc} \frac{B(y_2 - z_2)L}{cR} dz_2. \end{aligned} \quad (55)$$

The function μ is the effective backscattering reflectivity (not to be confused with $\nu(\mathbf{z})$) and can be thought of as a windowed Fourier transform of the actual reflectivity function ν on the Bragg wavenumber $2k_{\parallel}$, see [43] or [4, section 7.2]. Using these new notations and dropping the inessential factor of τ , one can reduce formula (53) to

$$\begin{aligned} u(x_1, y_2) &\approx \int \chi_{L_{\text{SA}}}(x_1 - z_1) \exp(-i\psi(x_1, z_1, y_2 - w_z)) \\ &\times \exp(i\omega_0(x_1 - z_1)^2 / (Rc)) \mu(z_1, y_2 - w_z) dz_1, \end{aligned} \quad (56)$$

where $w_z \equiv w(x_1, \mathbf{z}) = (x_1 - z_1)^2 / (2L)$.

At the second stage of the aforementioned three-stage process, the reconstruction phase $\psi_{\text{rec}}(x_1, \mathbf{y}) \equiv \psi_{\text{rec}}(x_1, y_1, y_2)$ is estimated. This step is the heart of autofocus, and several efficient reconstruction methods are available in the literature, see, e.g. [26–30]. The resulting estimate is used at the third stage where the image \mathcal{I} is obtained by matched filtering in the cross-range direction. We represent the latter procedure as follows:

$$\begin{aligned} \mathcal{I}(y_1, y_2) &= \int \chi_{L_{\text{SA}}}(x_1 - y_1) \exp(i\psi_{\text{rec}}(x_1, y_1, y_2 + w_y)) \\ &\times \exp(-i\omega_0(x_1 - y_1)^2 / (Rc)) u(x_1, y_2 + w_y) dx_1, \end{aligned} \quad (57)$$

where

$$w_y \equiv w(x, \mathbf{y}) = \frac{(x_1 - y_1)^2}{2L}, \quad w_z \equiv w(x_1, \mathbf{z}) = \frac{(x_1 - z_1)^2}{2L}, \quad (58)$$

and $\mathcal{I}(y_1, y_2) = I(y_1, y_2) \exp(2ik_{\parallel}y_2)$. Note that \mathcal{I} is also a slow function of y_2 .

A.2. Range cell migration and transition to two-dimensional formulation

Transition to the two-dimensional formulation (i.e. the one where functions \mathcal{I} , u , ψ , and ψ_{rec} are one-dimensional) would be simple if it were possible to ignore simultaneously the terms w_z and w_y in (56) and (57), respectively. Then, after dropping w_z and w_y , equations (56) and (57) for different values of y_2 would decouple. This decoupling allows one to remove y_2 from the

arguments of the above functions, which means that equations (56) and (57) are considered for a certain value of y_2 . However, it turns out that for typical SAR systems, ignoring w_z and w_y requires further justification. In particular, one should impose additional conditions on \mathcal{I} and μ and modify the definition of the antenna signal, as explained below.

The terms w_z and w_y in the arguments of μ , ψ , and ψ_{rec} in (56) and (57) yield a difference between the range coordinates on the left and right hand sides of these equations. This effect is called the range cell migration (RCM), see, e.g. [11], and its magnitude should be compared to the ground range resolution:

$$\Delta_{\text{Rg}} = \Delta_{\text{R}} R/L, \quad (59)$$

see figure 2, where $\Delta_{\text{R}} = \pi c/B$ is defined in (54). For example, the value of $|x_1 - z_1|$ in (56) is limited by $\chi_{L_{\text{SA}}}(x_1 - z_1)$ that represents the beam footprint: $|x_1 - z_1| \leq L_{\text{SA}}/2$. Then the inequality

$$\max |w_z| \leq \frac{\Delta_{\text{Rg}}}{2} \iff \frac{B}{\omega_0} \frac{L_{\text{SA}}^2}{2\lambda R} \leq 1 \quad (60)$$

can be understood as a condition for $u(x_1, y_2)$ in (56) to be affected by the values of μ in a single ground range bin of width Δ_{Rg} .

It turns out that for real-world SAR systems, condition (60) usually does not hold⁸. Hence, to calculate a single value of u , we should have defined μ in several adjacent range bins. Similarly, the signal processing procedure (57) should take RCM into account by using the values of u and ψ_{rec} from several adjacent range bins in order to calculate a single value of \mathcal{I} . Accordingly, the purpose of the term w_y in this formula is to compensate for RCM in the signal. In the presence of phase perturbations, the function $\Psi(\mathbf{s})$ should be defined in a band of width $\max |w_z| \cdot \xi$ in the range direction. Note that ignoring RCM in (57) yields the so-called ‘Unfocused SAR’, see [11, section 5.7.3], that even in the absence of phase perturbations exhibits inferior resolution as compared to the regular SAR processing given by (7) with $\psi_{\text{rec}} \equiv 0$.

The actual obstacle to building a two-dimensional representation for equations (56) and (57) is the dependence of the RCM terms on x_1 and y_1 , respectively. For example, dropping temporarily ψ_{rec} from (57), we can fix $y_2 = y_2^s$, define a function of one argument $\mathcal{I}^s(y_1) \stackrel{\text{def}}{=} \mathcal{I}(y_1, y_2^s)$, and then choose certain y_1 to define $u^s(x_1)$ as $u(x_1, y_2^s + (y_1 - x_1)^2/(2L))$. Then equation (57) can be seen as a formula for $\mathcal{I}^s(y_1)$ that involves another function of one argument, i.e. $u^s(x_1)$; however, doing so for a different value of y_1 requires redefinition of u^s . We can choose not to redefine u^s but rather use one and the same function $u^s(x_1)$ for some or all other values of y_1 claiming that $u(\cdot, \cdot)$ is a slow function in its second argument, see (55). As, however, the condition (60) does not hold, this will not be valid for all pairs (x_1, y_1) related by formula (57).

Yet it is possible to satisfy the first inequality in (60) if we calculate the image $\mathcal{I}(y_1, y_2)$ for a fixed $y_2 = y_2^s$ while restricting y_1 to a segment with the length significantly smaller than L_{SA} . Specifically, let

$$\underline{\mathbf{S}} = \{y_1 \mid |y_1 - x_1^s| \leq S/2\}, \quad \underline{\mathbf{F}} = \{x_1 \mid |x_1 - x_1^s| \leq L_{\text{SA}}/2\}, \quad (61)$$

where x_1^s and S are the reference azimuthal coordinate and width of the segment $\underline{\mathbf{S}}$, respectively. Next, we define

$$u^s(x_1) \stackrel{\text{def}}{=} u\left(x_1, y_2^s + \frac{(x_1 - x_1^s)^2}{2L}\right) \quad (62)$$

⁸ For example, the resolution of the BIOMASS single look complex (SLC) images [47] indicates that the value of $\max |w_z|/(\Delta_{\text{Rg}}/2)$ exceeds 10.

and emphasize that $u^s(x_1)$ given by (62) does not depend on y_1 . If we use $u^s(x_1)$ instead of $u(x_1, y_2)$ in (57) to calculate $\mathcal{I}(y_1, y_2^s)$ for $y_1 \in \underline{\mathbf{S}}$, we should require that

$$u\left(x_1, y_2^s + \frac{(x_1 - x_1^s)^2}{2L}\right) \approx u\left(x_1, y_2^s + \frac{(x_1 - y_1)^2}{2L}\right) \quad \text{for all } y_1 \in \underline{\mathbf{S}}, \quad x_1 \in \underline{\mathbf{F}}. \quad (63)$$

The approximate equality in (63) is understood similarly to (60): given that the spatial scale of variation of u with respect to its second argument is Δ_{Rg} , see (55) and (59), we assume that (63) is satisfied if

$$\left| \frac{(x_1 - x_1^s)^2}{2L} - \frac{(x_1 - y_1)^2}{2L} \right| \leq \frac{\Delta_{Rg}}{2} \quad \text{for all } y_1 \in \underline{\mathbf{S}}, \quad x_1 \in \underline{\mathbf{F}}. \quad (64)$$

Taking into account the definitions (61), we rewrite this condition as

$$S \leq 2\Delta_R \frac{R}{L_{SA}} \iff \frac{S}{\Delta_A} \leq 2 \frac{\Delta_R}{\Delta_A} \frac{R}{L_{SA}}. \quad (65)$$

For the function $u^s(x_1)$ defined in (62), formula (56) yields:

$$u^s(x_1) = \int \chi_{L_{SA}}(x_1 - z_1) \exp(-i\psi(x_1, z_1, y_2^s)) \times \exp(i\omega_0(x_1 - z_1)^2 / (Rc)) \mu(z_1, y_2^s) dz_1, \quad (66)$$

where

$$y_2^s = y_2^s + \frac{(x_1 - x_1^s)^2}{2L} - \frac{(x_1 - z_1)^2}{2L}. \quad (67)$$

Our next step is to specify a one-dimensional function $\mu^s(z_1)$ that will be related to $u^s(x_1)$ via a one-dimensional counterpart to (66). We do so by restricting the support of μ^s :

$$\mu^s(z_1) \stackrel{\text{def}}{=} \begin{cases} \mu(z_1, y_2^s) & \text{if } z_1 \in \underline{\mathbf{S}}, \\ 0 & \text{otherwise.} \end{cases} \quad (68)$$

Then, if the values of y_2^s in (62) and (68) are the same, replacing $\mu(z_1, y_2^s)$ in (66) with $\mu^s(z_1)$ is possible as long as (see (67))

$$\mu(z_1, y_2^s) \approx \mu\left(z_1, y_2^s + \frac{(x_1 - x_1^s)^2}{2L} - \frac{(x_1 - z_1)^2}{2L}\right) \quad \text{for all } z_1 \in \underline{\mathbf{S}}, \quad x_1 \in \underline{\mathbf{F}}. \quad (69)$$

The scale of variation of μ in its second argument is Δ_{Rg} , similarly to that of u , see (53)–(55), and the condition for (69) to hold can be obtained from (64) by replacing y_1 with z_1 . We see that for μ^s defined as in (68), this condition is satisfied.

For $\psi(x_1, z_1, y_2') = \Psi(\mathbf{s}(x_1, z_1, y_2'))$ in equation (56), where

$$\mathbf{s}(x_1, z_1, y_2') = (\xi x_1 + (1 - \xi)z_1, -\xi L + (1 - \xi)y_2'),$$

see (8), we define the two-dimensional representation as

$$\psi^s(x_1, z_1) = \Psi(\mathbf{s}^s(x_1, z_1)), \quad \text{where } \mathbf{s}^s = (\xi x_1 + (1 - \xi)z_1, -\xi L + (1 - \xi)y_2^s).$$

With the scale of variation of Ψ denoted by $\mathcal{L} = l\Delta_A$, see (10), we consider this substitution valid as long as

$$\xi \frac{SL_{SA}}{4L} \leq \mathcal{L} \iff \frac{S}{\Delta_A} \leq \frac{l}{\xi} \frac{4L}{L_{SA}}. \quad (70)$$

The conditions imposed on S by (65) and (70) should be considered in the context of the focusing procedure described in section 5. This procedure is based on a system of point scatterers (29) as a model of reflectivity, more specifically—on a pair of point scatterers in a single range bin with the dimensionless azimuthal coordinates satisfying condition (41). Moreover, the vertical focusing uses CINT images $Y(\mathbf{y}_a, \mathbf{y}_b)$ rather than regular SAR images $\mathcal{I}(\mathbf{y})$. Hence, we should demonstrate that this technique can be realized via the new functions and within the specified limitations.

First, we observe that if \mathbf{y}_a and \mathbf{y}_b are simultaneously in one range bin and in one azimuthal segment as described above, then they share the values of x_1^s and y_2^s , and hence, the set of functions $(\mathcal{I}^s, u^s, \mu^s, \psi^s)$. This allows us to express $\mathcal{I}^s(y_{a1})\overline{\mathcal{I}^s(y_{b1})}$ as a double integral over $dx_{a1}dx_{b1}$. As explained in detail in section 3, the expression for the CINT image $Y^s(y_{a1}, y_{b1})$ is obtained from that for $\mathcal{I}^s(y_{a1})\overline{\mathcal{I}^s(y_{b1})}$ by modifying the signal processing (i.e. integration) domain:

$$\begin{aligned} & \text{supp}_{(x_{a1}, x_{b1})} (\chi_{L_{SA}}(x_{a1} - y_{a1})\chi_{L_{SA}}(x_{b1} - y_{b1})) \\ & \quad \downarrow \\ & \text{supp}_{(x_{a1}, x_{b1})} (\chi_{L_{SA}}(x_{a1} - y_{a1})\chi_{L_{SA}}(x_{b1} - y_{b1})\chi_{l\Delta_A}(x_{a1} - x_{b1})) \end{aligned}$$

see (21). Then we remind that the focusing procedure requires that the azimuthal coordinates of the pair of point scatterers satisfy $|z_{a1} - z_{b1}| \gg \mathcal{L}$, which corresponds to $|z_{\beta}^{\text{PS}} - z_{\alpha}^{\text{PS}}| \gg l$ in dimensionless coordinates, see (41). We can see that this is achievable (i.e. does not contradict (65) and (70)) because for a typical SAR system $\Delta_R \sim \Delta_A$ and $\xi \sim 0.5$, whereas $L_{SA} \ll R \sim L$ and $l \gg 1$. Hence, we can use Y^s , u^s , μ^s , and ψ^s for modeling of the vertical focusing procedure as described in sections 5 and 6.

Note that condition (65) on S can be relaxed by reducing the system bandwidth, thus increasing the value of Δ_R . Additionally, adoption of a larger value of Δ_R increases the chances of finding a suitable pair of point scatterers within a single range bin. Possible adverse effects of reduced bandwidth (e.g. a drop in the signal-to-noise ratio), as well as the effects of scatterers beyond the specified segments, have to be studied separately.

Table 3. Coefficients in formula (46) for different realizations of the phase screen in figure 12. The values of k_n and a_n are the same as in table 2.

k_n	a_n	realization A		realization B		realization C	
		p_n	q_n	p_n	q_n	p_n	q_n
0.32044	0.79698	-0.77579	-0.18255	-0.06660	-0.79419	0.35860	0.71175
0.42726	0.44830	-0.07031	0.44275	-0.43827	0.09433	0.43796	0.09573
0.53407	0.28691	-0.25160	-0.13790	0.28571	-0.02624	0.28267	0.04915
0.64088	0.19925	-0.19841	-0.01822	0.17384	0.09736	-0.19078	-0.05745
0.74770	0.14638	0.14591	-0.01174	0.11881	0.08551	-0.11335	0.09263
0.85451	0.11208	-0.11172	-0.00888	0.10961	-0.02336	0.01790	0.11064
0.96133	0.08855	0.08270	0.03166	0.08533	0.02366	-0.05575	0.06880

Assuming that the condition (65) is satisfied, we present the resulting system as follows:

$$u^s(x_1) = \int \chi_{L_{SA}}(x_1 - z_1) \exp(-i\psi^s(x_1, z_1)) \times \exp(i\omega_0(x_1 - z_1)^2/(Rc)) \mu^s(z_1) dz_1, \quad (71)$$

$$\mathcal{I}^s(y_1) = \int \chi_{L_{SA}}(x_1 - y_1) \exp(i\psi_{rec}^s(x_1, y_1)) \times \exp(-i\omega_0(x_1 - y_1)^2/(Rc)) u^s(x_1) dx_1. \quad (72)$$

By dropping the superscript ‘s’ and performing transition to dimensionless coordinates as described in section 2.2, we simplify these equations further to system (11) and (12) in the main text.

Appendix B. Parameter study

In this appendix, we illustrate how varying some problem parameters affects the CINT image described in section 3 and the focusing procedure developed in section 5.

Figures 12–14 contain fragments from CINT images similar to those in figure 10. Figure 12 presents three different realizations of the ionospheric screen, with a separate plot displaying all three realizations of $\Psi(s)$. The values of the parameters k_n , p_n , and q_n for these realizations are listed in table 3. Figure 13 demonstrates the effect of the perturbation amplitude a_{scr} , see (46). Figure 14 allows us to compare the plots of $\mathcal{Y}(y_D; \xi)$ for different values of the grid step used for discretization of the scatterer, data, and image.

Figures 15 and 16 are similar to figure 11: the plots of $\mathcal{Y}(y_D; \xi)$ and $\mathcal{P}(\xi)$ illustrate the focusing procedure of section 5. Figure 15 demonstrates the effect of the noise level by varying the parameter p_{noise} , see (14): we see that the method can withstand a significant additive noise. Figure 16 shows focusing for different distances within the pair of scatterers that generate the streak used in the focusing procedure of section 5. These distances are given by $|z_b^{PS} - z_a^{PS}|$, see (30) and section 6. In our simulation, we varied the location of the first point scatterer, i.e. z_a^{PS} .

Overall, figures 12–16 demonstrate a reasonable level of stability of the CINT images and focusing procedure to variations of the problem parameters.

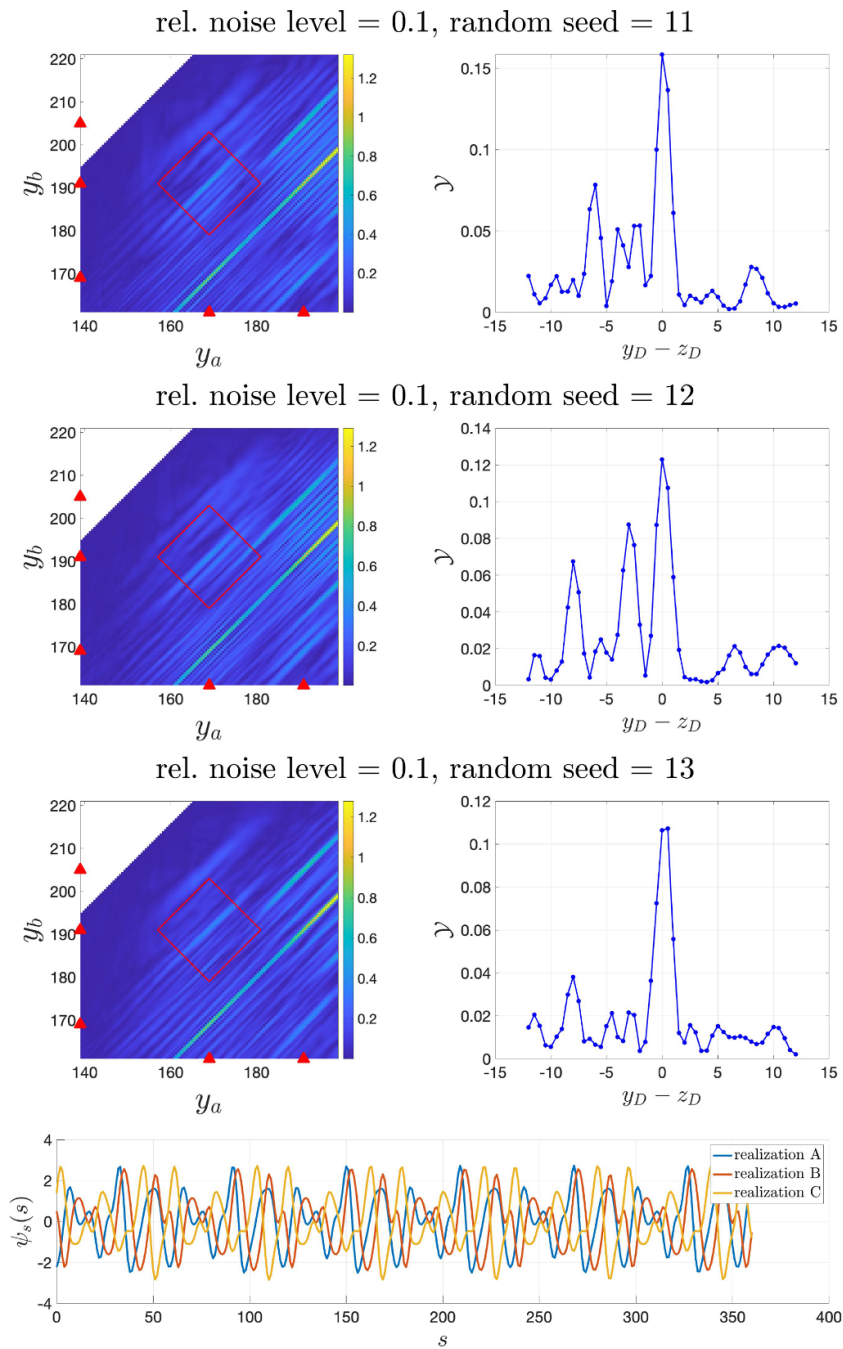


Figure 12. Appearance of the CINT image streaks for different realizations of the ionospheric phase screen for $\xi_0 = 0.5$ and $\xi = 0.54$. The values of p_n and q_n for each realization of the phase screen density function, see formula (46), are listed in table 3. The bottom panel plots all three realizations of $\Psi(s)$.

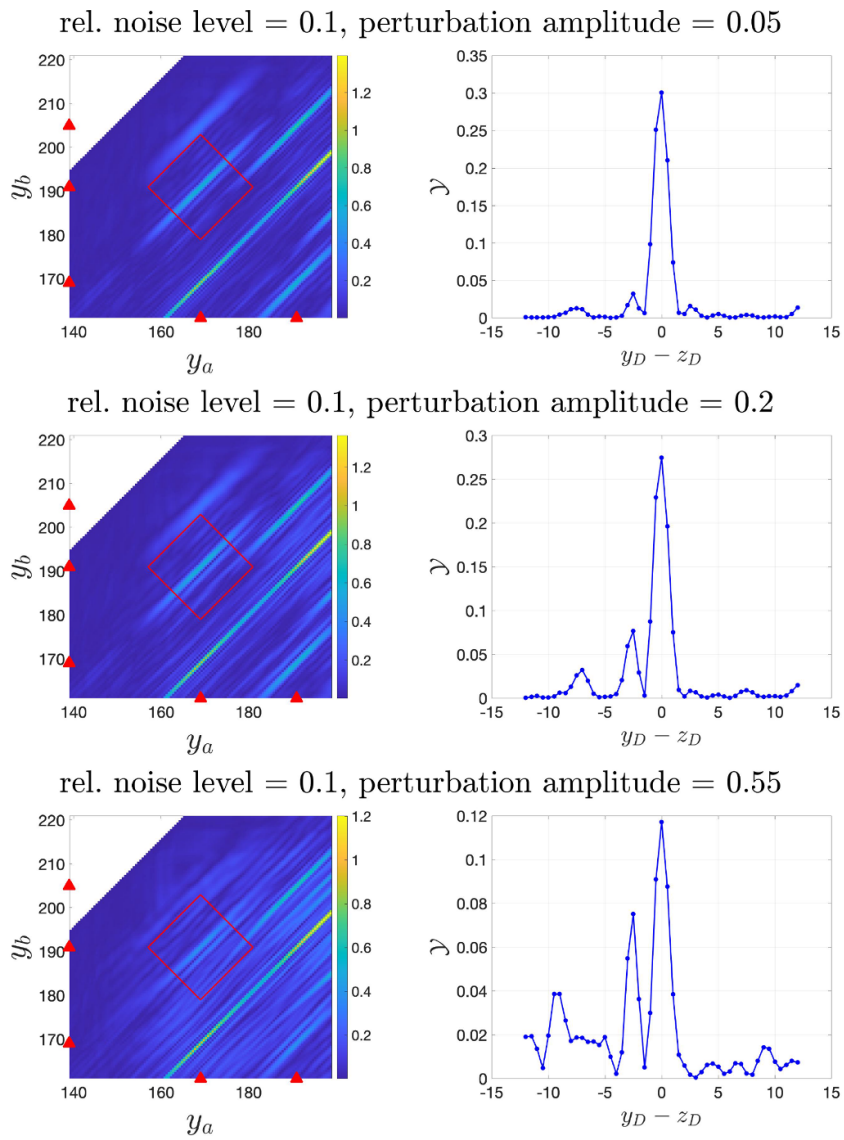


Figure 13. Effect of the perturbation amplitude a_{scr} , see (46), for $\xi_0 = 0.5$ and $\xi = 0.54$, on the appearance of streaks in the CINT image.

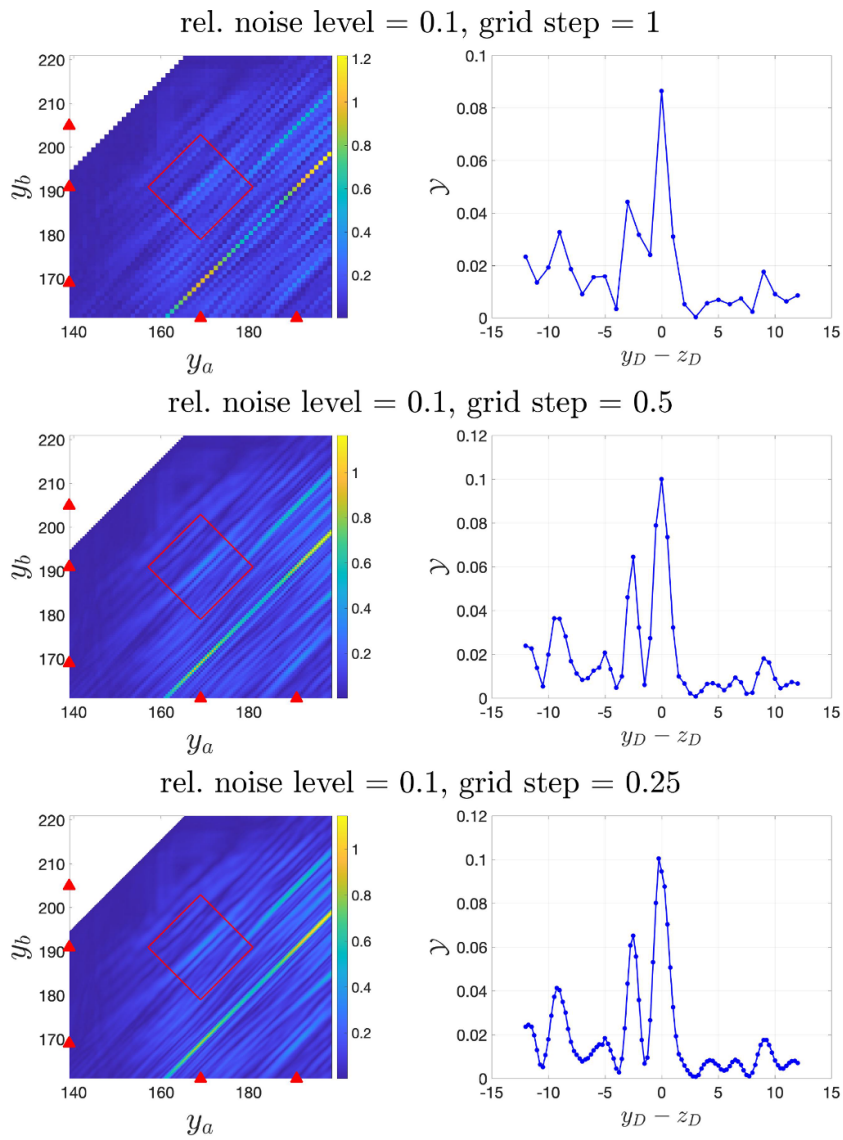


Figure 14. Effect of the discretization for $\xi_0 = 0.5$ and $\xi = 0.54$ on the appearance of streaks in the CINT image. The grid step is the same for x , y , and z .

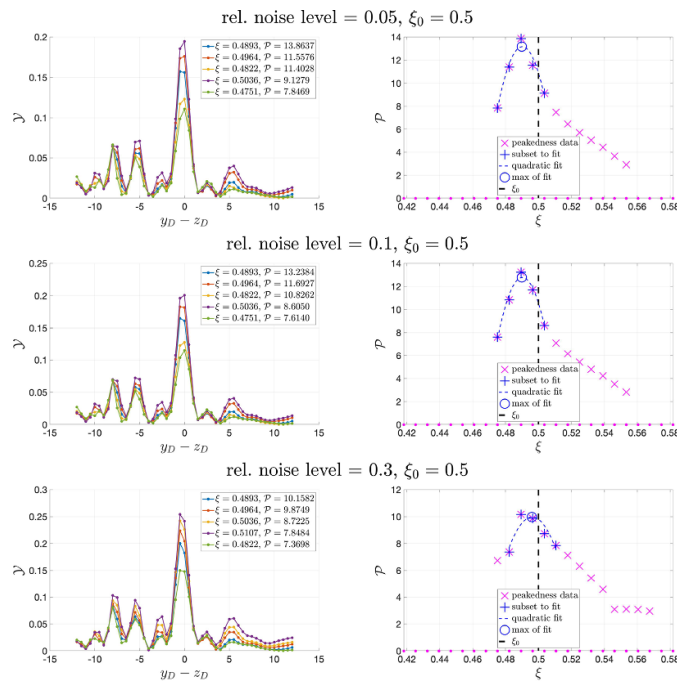


Figure 15. Effect of the noise level (i.e. the value of p_{noise} in (14)) on the focusing procedure.

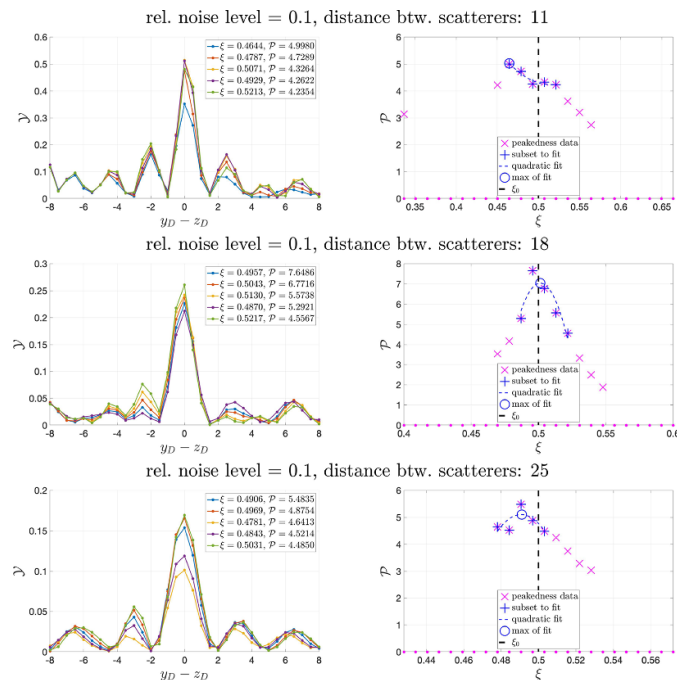


Figure 16. Effect of the distance within the pair of point scatterers that yield the focusing streak, see (30), on the focusing procedure.

ORCID iDs

Mikhail Gilman  <https://orcid.org/0000-0001-6970-627X>

Semyon Tsynkov  <https://orcid.org/0000-0003-1069-9612>

References

- [1] Moreira A, Prats-Iraola P, Younis M, Krieger G, Hajnsek I and Papathanassiou K P 2013 A tutorial on synthetic aperture radar *IEEE Geosci. Remote Sens. Mag.* **1** 6–43
- [2] Meyer F, Bamler R, Jakowski N and Fritz T 2006 The potential of low-frequency SAR systems for mapping ionospheric TEC distributions *IEEE Geosci. Remote Sens. Lett.* **3** 560–4
- [3] Kim J S, Papathanassiou K P, Scheiber R and Quegan S 2015 Correcting distortion of polarimetric SAR data induced by ionospheric scintillation *IEEE Trans. Geosci. Remote Sens.* **53** 6319–35
- [4] Gilman M, Smith E and Tsynkov S 2017 *Transionospheric Synthetic Aperture Imaging (Applied and Numerical Harmonic Analysis)* (Cham: Birkhäuser/Springer)
- [5] Smith E M and Tsynkov S V 2011 Dual carrier probing for spaceborne SAR imaging *SIAM J. Imaging Sci.* **4** 501–42
- [6] Gilman M, Smith E and Tsynkov S 2013 Reduction of ionospheric distortions for spaceborne synthetic aperture radar with the help of image registration *Inverse Problems* **29** 054005
- [7] Gilman M and Tsynkov S 2017 Mathematical analysis of SAR imaging through a turbulent ionosphere *AIP Conf. Proc.* **1895** 020003
- [8] Le Toan T *et al* 2011 The BIOMASS mission: mapping global forest biomass to better understand the terrestrial carbon cycle *Remote Sens. Environ.* **115** 2850–60
- [9] Heliere F, Fois F, Arcioni M, Bensi P, Fehring M and Scipal K 2014 Biomass P-band SAR interferometric mission selected as 7th Earth Explorer Mission *Proc. EUSAR 2014; 10th European Conf. on Synthetic Aperture Radar (VDE)* pp 1–4
- [10] Cheney M 2001 A mathematical tutorial on synthetic aperture radar *SIAM Rev.* **43** 301–12
- [11] Cumming I G and Wong F H 2005 *Digital Processing of Synthetic Aperture Radar Data. Algorithms and Implementation* (Boston, MA: Artech House)
- [12] Blaustein N and Plohotniuc E 2008 *Ionosphere and Applied Aspects of Radio Communication and Radar* (Boca Raton, FL: CRC Press/Taylor & Francis)
- [13] Gracheva V, Kim J S, Prats-Iraola P, Scheiber R and Rodriguez-Cassola M 2021 Combined estimation of ionospheric effects in SAR images exploiting Faraday rotation and autofocus *IEEE Geosci. Remote Sens. Lett.* **19** 8018705
- [14] Pi X, Freeman A, Chapman B, Rosen P and Li Z 2011 Imaging ionospheric inhomogeneities using spaceborne synthetic aperture radar *J. Geophys. Res.* **116** 1–13
- [15] Garnier J and Sølna K 2008 Coherent interferometric imaging for synthetic aperture radar in the presence of noise *Inverse Probl.* **24** 055001
- [16] Borcea L and Garnier J 2020 High-resolution interferometric synthetic aperture imaging in scattering media *SIAM J. Imaging Sci.* **13** 291–316
- [17] Borcea L and Garnier J 2021 Imaging in random media by two-point coherent interferometry *SIAM J. Imaging Sci.* **14** 1635–68
- [18] Borcea L, Papanicolaou G and Tsogka C 2006 Coherent interferometric imaging in clutter *Geophysics* **71** S1165–75
- [19] Brcic R, Parizzi A, Eineder M, Bamler R and Meyer F 2011 Ionospheric effects in SAR interferometry: an analysis and comparison of methods for their estimation *Proc. 2011 IEEE Int. Geoscience and Remote Sensing Symp. (IGARSS'11) (Vancouver, Canada, July 2011)* (IEEE) pp 1497–500
- [20] Knepp D L and Groves K M 2013 The effect of ionospheric scintillation on phase gradient autofocus processing of synthetic aperture radar *2013 7th European Conf. on Antennas and Propagation (EuCAP)* (IEEE) pp 3664–7
- [21] Li Z, Quegan S, Chen J and Rogers N C 2015 Performance analysis of phase gradient autofocus for compensating ionospheric phase scintillation in BIOMASS P-band SAR data *IEEE Geosci. Remote Sens. Lett.* **12** 1367–71
- [22] Gomba G, Parizzi A, De Zan F, Eineder M and Bamler R 2015 Toward operational compensation of ionospheric effects in SAR interferograms: the split-spectrum method *IEEE Trans. Geosci. Remote Sens.* **54** 1446–61

- [23] Wang C, Chen L, Zhao H, Lu Z, Bian M, Zhang R and Feng J 2017 Ionospheric reconstructions using Faraday rotation in spaceborne polarimetric SAR data *Remote Sens.* **9** 1169
- [24] Chen J and Zebker H A 2012 Ionospheric artifacts in simultaneous L-band InSAR and GPS observations *IEEE Trans. Geosci. Remote Sens.* **50** 1227–39
- [25] Zhang B 2016 Three methods to retrieve slant total electron content measurements from ground-based GPS receivers and performance assessment *Radio Sci.* **51** 972–88
- [26] Jakowatz C V Jr, Wahl D E, Eichel P H, Ghiglia D C and Thompson P A 1996 *Spotlight-Mode Synthetic Aperture Radar: A Signal Processing Approach* (Berlin: Springer)
- [27] Warner D W, Ghiglia D C, Fitzgerrell A and Beaver J 2000 Two-dimensional phase gradient autofocus *Proc. SPIE* **4123** 162–73
- [28] Scarnati T and Gelb A 2018 Joint image formation and two-dimensional autofocusing for synthetic aperture radar data *J. Comput. Phys.* **374** 803–21
- [29] Callow H J, Hayes M P and Gough P T 2003 Stripmap phase gradient autofocus *Oceans 2003. Celebrating the Past... Teaming Toward the Future (IEEE Cat. No. 03CH37492)* vol 5 (IEEE) pp 2414–21
- [30] Wahl D E, Jakowatz C V Jr, Thompson P A and Ghiglia D C 1994 New approach to strip-map SAR autofocus *6th IEEE Digital Signal Processing Workshop, 1994* (IEEE) pp 53–56
- [31] Gilman M and Tsynkov S 2022 A mathematical perspective on radar interferometry *Inverse Problems Imaging* **16** 119–52
- [32] Bamler R and Hartl P 1998 Synthetic aperture radar interferometry *Inverse Problems* **14** R1
- [33] Rosen P A, Hensley S, Joughin I R, Li F K, Madsen S N, Rodriguez E and Goldstein R M 2000 Synthetic aperture radar interferometry *Proc. IEEE* **88** 333–82
- [34] Reigber A and Moreira A 2000 First demonstration of airborne SAR tomography using multi-baseline L-band data *IEEE Trans. Geosci. Remote Sens.* **38** 2142–52
- [35] Ferretti A, Prati C and Rocca F 2001 Permanent scatterers in SAR interferometry *IEEE Trans. Geosci. Remote Sens.* **39** 8–20
- [36] Crosetto M, Monserrat O, Cuevas-González Mia, Devanthery Nuria and Crippa B 2016 Persistent scatterer interferometry: a review *ISPRS J. Photogramm. Remote Sens.* **115** 78–89
- [37] Zhu X X, Wang Y, Montazeri S and Ge N 2018 A review of ten-year advances of multi-baseline SAR interferometry using TerraSAR-X data *Remote Sens.* **10** 1374
- [38] Cloude S 2010 *Polarisation: Applications in Remote Sensing* (Oxford: Oxford University Press)
- [39] Garnier J and Sølna K 2013 A multiscale approach to synthetic aperture radar in dispersive random media *Inverse Problems* **29** 054006
- [40] Belcher D P and Rogers N C 2009 Theory and simulation of ionospheric effects on synthetic aperture radar *IET Radar Sonar Navig.* **3** 541–51
- [41] Meyer F J 2014 Quantifying ionosphere-induced image distortions in L-band SAR data using the ionospheric scintillation model WBMOD *Proc. EUSAR 2014; 10th European Conf. on Synthetic Aperture Radar* (VDE) pp 1–4
- [42] Born M and Wolf E 1999 *Principles of Optics: Electromagnetic Theory of Propagation, Interference and Diffraction of Light* 7th (expanded) edn ed A B Bhatia, P C Clemmow, D Gabor, A R Stokes, A M Taylor, P A Wayman and W L Wilcock (Cambridge: Cambridge University Press)
- [43] Gilman M and Tsynkov S 2015 A mathematical model for SAR imaging beyond the first Born approximation *SIAM J. Imaging Sci.* **8** 186–225
- [44] Colton D and Kress R 2013 *Inverse Acoustic and Electromagnetic Scattering Theory (Applied Mathematical Sciences vol 93)* 3rd edn (New York: Springer)
- [45] Capozzoli A, Curcio C and Liseno A 2013 Experimental field reconstruction of incoherent sources *Prog. Electromagn. Res. B* **47** 219–39
- [46] Oliver C and Quegan S 1998 *Understanding Synthetic Aperture Radar Images (Artech House Remote Sensing Library)* (Boston, MA: Artech House)
- [47] Banda F *et al* 2020 The BIOMASS level 2 prototype processor: design and experimental results of above-ground biomass estimation *Remote Sens.* **12** 985